

Heat transfer enhancement in counter-flow-heat-exchanger for use in micro-fabricated Joule- Thomson cryocooler

Fraiman Leonid

פריימן לאוניד

Heat transfer enhancement in counter-flow-heat-exchanger for use in micro-fabricated Joule-Thomson cryocooler

Research Thesis

In Partial Fulfillment of the Requirements for the
Degree of Master of Science in Mechanical Engineering

Fraiman Leonid

Submitted to the Senate of the Technion – Israel Institute of
Technology

Kislev, 5777

Haifa

December, 2016

ACKNOWLEDGMENTS

This research thesis was done under the supervision of Associate Professor Gilad Yossifon, Head of the Micro- and Nanofluidics Laboratory in the Faculty of Mechanical Engineering. The research was financially supported by the Technion - Norman and Helen Asher Space Research Institute (ASRI), Technion Funds for Security Research (CSST) and Rafael Advanced Defense Systems Ltd. The fabrication of the chip was made possible through the technical support of the micro- and Nanofluidics technical staff and the Technion Russell Berrie Nanotechnology Institute and Micro Nano-Fabrication Unit. The assistance of all above is gratefully acknowledged.

PUBLICATIONS

1. Conference Presentation:

1.1. **L. Fraiman**, A. Parahovnik, I. Rosinsky and G. Yossifon

“Heat transfer enhancement in counter-flow-heat-exchanger for use in micro fabricated Joule-Thomson cryocooler”, 5th Micro and Nano Flows Conference, Milan, Italy, 11-14 September 2016.

2. Scientific journal papers:

2.1. A. Parahovnik, **L. Fraiman**, I. Rosinsky and G. Yossifon, "Temperature and high pressure effects on choked flow in the microchannel," *Physics of fluids* 28, 02205, 2016.

2.2. **L. Fraiman**, A. Parahovnik, I. Rosinsky and G. Yossifon, “Geometrical optimization of counter-flow heat exchanger integrated within a microfabricated Joule-Thomson cryocooler (submitted).

TABLE OF CONTENTS

1	Introduction to Joule-Thomson cryocoolers	7
1.1	Working principle	7
1.2	Setting the operating conditions	8
1.3	Heat exchanger design approaches.....	10
1.4	Motivation and studies objectives	11
2	Theoretical methodology	12
2.1	Scaling effects.....	12
2.2	Correlations for heat transfer coefficient and pressure drop	13
2.3	Heat exchanger and cooler effectiveness relations.....	15
3	Optimization methodology.....	18
3.1	Optimization need justification	18
3.2	Optimization scheme	19
3.3	Optimization results.....	20
4	CFD analysis methodology	22
4.1	Computational model	22
4.2	Model validation	23
4.3	Verification of optimum geometry and mass flow rate.....	24
5	Experimental methodology.....	26
5.1	Chip design and fabrication.....	26
5.2	Test bench design.....	27
6	Results and discussion	29
7	Conclusions and future work.....	33
8	References.....	35
	Appendixes.....	37
	APPENDIX A – General supplementary information	37
	APPENDIX B – Material properties.....	39
	APPENDIX C – Estimation of radiative heat transfer interaction	42
	APPENDIX D – The NTU method	44
	APPENDIX E – Structural strength analysis	46
	Appendix F – Chip manufacturing	48

LIST OF FIGURES

- Figure 1 | (a) Schematics of the Joule-Thomson cryocooler. The device has three main parts: counter-flow heat exchanger – used for coolant precooling prior entering the orifice, orifice where isenthalpic expansion (i.e. JT effect) takes place and the heat absorption area (HAA) containing the liquefied nitrogen (in case liquefaction conditions are reached) and absorbing heat from the device that is being cooled. (b) Microscopic image (top-view) of the device; (c) Schematics of the periodic unit cell of the HE channel of total width w_{HE} and length L_{HE} . There are two straight and opposite flow channels one above the other corresponding to the high and low pressure streams, both having the same unit cell width S_w but can have different pin diameter, d , and channel height, y 7
- Figure 2 | A variety of heat exchangers configurations studied throughout the years. (a) tube and shell, (b) meandering pipes, (c) porous pipe, (d) parallel channels with micro-pins, (e) spirals and (f) plates stack.10
- Figure 3 | Cooler effectiveness dependency on heat exchanger effectiveness for constant inlet conditions. It is noted that for HE effectiveness values below 88[%] saturation conditions cannot be reached.....16
- Figure 4 | Trends of parameters behavior for achieving desired problem quantities, at low pressure and temperature stream. (a) Pressure losses map, plotted for variable values of channel height, y_L , pin diameter, d_L , and coolant mass flow rate, m . Lower (desirable) values are obtained for largest channel height and smallest mass flow rates; (b) Convection heat transfer coefficient map, plotted for the same variable parameters. Higher (desirable) values are obtained for smallest channel height and largest mass flow rates.....18
- Figure 5 | Computational model of the periodic unit cell simulated in Fluent and consisting of the high and low fluid streams and the separating wall. Surfaces pointing in the directions Z and Y are thermally insulated due to the low thermal conductivity of the contacting glass which is omitted from the model while the surfaces pointing in the direction X obeys symmetry conditions. ...22
- Figure 6 | Relative effectiveness dependency on the separating wall thermal conductivity. Maximum performance is achieved for thermal conductivity of $\sim 2\text{-}3 \text{ [Wm}^{-1}\text{K}^{-1}]$ and in agreement with previous studies [15].25
- Figure 7 | Schematics of the experimental setup. The coolant is supplied from a N_2 vessel and its pressure controlled using a pressure regulator that is assembled on the supply line before the device inlet (point 1) along with pressure, temperature and mass flow rate gauges. To reduce the heat interaction of the device with the environment the entire device was under vacuum and fixed by a special holder which also have role of an inlet and outlet manifold. In addition, temperature measurements point 3 and 4 were obtained using externally (to the glass) bonded thermocouples.....27
- Figure 8 | Comparison of the CFD and experimental results. (a) Cooling effect achieved in the experiments, defined by the temperature difference between the inlet and heat absorption area wall, versus the inlet pressure. It is noted that the cooling effect is increasing with increasing inlet pressure. The error range presented is $\pm 1[^\circ\text{C}]$, which is maximum estimated absolute error between the

experimental data and numerical simulation. The two points marked by red crosses represent experiments where ideal insulation assumption has been violated. (b) Cooler effectiveness dependence on HE effectiveness, where every point stands for a different experiment. This, nonlinear behavior, differs from one presented in Figure 3, since each experiment has a new set of inlet conditions. CFD analysis results lie in the 3[%] maximum absolute error range from the experimental data excluding two points marked by big red crosses, presenting experiments where ideal insulation assumption is violated.....31

Figure A-1 | Axial heat conduction effect within the separating wall of a microscale heat exchanger. The HE effectiveness value depends on the wall material conductivity. Optimal performance achieved for wall made of glass like materials, having thermal conductivity of about 1 [Wm⁻¹K⁻¹]......38

Figure B-1 | Nitrogen density for (a) high and (b) low stream, 2300[psia] and 20[psia] respectively. It is noted that ideal gas assumption is holding for the low stream, while for the high stream it produces significant error, [28]......40

Figure B-2 | Nitrogen specific heat capacity for (a) high and (b) low stream, 2300[psia] and 20[psia] respectively. It is noted that high pressure stream have higher heat capacity at all considered temperatures, [28]......40

Figure B-3 | Nitrogen thermal conductivity for (a) high and (b) low stream, 2300[psia] and 20[psia] respectively, [28]......41

Figure B-4 | Nitrogen dynamic viscosity for (a) high and (b) low stream, 2300[psia] and 20[psia] respectively, [28]......41

Figure C- 1 | Radiation heat transfer interaction during the performed tests. At experiments with low operating pressure, 54 and 97 [psig], the radiative losses are significant, therefore the perfect insulation assumption, at these experiments does not hold42

Figure D-1 |Schematics of the HE part of the device for which heat balance calculation performed.45

Figure F-1 | The effect of the exposure time of the wafer to HF acid at 49[%] concentration: (a) Exposure of 60 [sec], results in high quality circular pins. (b) Exposure of 90 [sec], results in degradation of the pins round shape.48

Figure F-2 | The various parts of the microcooler assembly. Bottom – contains the low stream channel and pins, middle – plain piece of glass serves as both the separating wall and expansion chamber where heat absorption occurs. Top – containing the high stream channel with structural pins and additional straight and narrow channels (orifices) for the throttling process. The rightmost part depicted the assembled device.48

LIST OF TABLES

Table 1 Summary of boundary conditions at HE's ports, Figure 1a.....	9
Table 2 Results of the optimization procedure obtained using the approximate solution.....	20
Table 3 CFD solution verification by compare against approximate solution basing on experimental and analythical correlations.	23
Table 4 Verification of optimization results by CFD analysis	24
Table 5 Detailed listing of experiments conducted on first prototype.....	29
Table A-1 Flow regimes classification based on the value of the Knudsen number [27].....	37
Table A-2 Heat transfer convection coefficient and fluid flow friction factor for fully developed laminar flow in ducts of various cross sections. Average Nusselt numbers are based on the cross sectional hydraulic diameter [18].	37
Table A-3 List of parameters influencing the microcooler performance.	38
Table B-1 Various combinations of nitrogen initial conditions at point 2 (Figure 1a), that are required for isenthalpic expansion that leads to coolant liquefaction at point 3 with ~ 80 [K] and ~ 0 [psig], [28].	39
Table B-2 Schott D 263® T ECO glass properties, [16].....	39

ABSTRACT

IR imaging systems require a low cost, small scale and reliable cooling device for maintaining a cryogenic temperature on the detector matrix, for achieving valuable image quality. Joule-Thomson (JT) cryo-cooler is a well-known device, designed to achieve coolant liquefaction at a constant cryogenic temperature at its cold tip. In the current work, we studied the performance of microscale JT cooler with integrated microscale counter-flow heat-exchanger (μ CFHE) having an array of structural pins and operating using nitrogen gas. Scaling effects, associated with micro-scale flow and heat transfer, were examined and properly treated. The geometry of the μ CFHE and mass flow rate were optimized to produce the maximum cooling power under the limitation of device inner pressure drop for achieving coolant liquefaction conditions. The optimization procedure consisted first on an approximate solution using the NTU method with experimentally derived correlations for the convective heat transfer coefficients obtained from the literature. Then, the optimization results were supported by computational fluid dynamics (CFD) analysis performed using ANSYS Fluent software. The proposed device prototype was built from three layers of glass slides using photolithographic micromachining process incorporating wet etching process, followed by glass-glass specially adapted thermal bonding procedure. The performance of such glass made cooler were investigated using a specially designed experimental setup and compared against both approximate solution and numerical simulation data, and were found to be in good agreement. Thus, validating the proposed generic optimization technique which can be applied for various microscale heat-exchanger designs.

ABBREVIATIONS

μ CFHE – micro CFHE

μ JT – micro JT

Bi – Biot number

CAE – Computer Aided Engineering

CFD – Computational Fluid Dynamics

CFHE – Counter Flow Heat Exchanger

FEA – Finite Elements Analysis

HAA – Heat Affected Area

HE – Heat Exchanger

HF – HydroFluoric acid

JT – Joule-Thomson

Kn – Knudsen number

M – Maranzana number

Ma – Mach number

NS – Navier-Stokes equations

NTU – Number of Transfer Units

Nu – Nusselt number

Re – Reynolds number

SD – Simultaneously Developing

TD – Thermally Developing

1 INTRODUCTION TO JOULE-THOMSON CRYOCOOLERS

1.1 WORKING PRINCIPLE

The performance of today highly compact packaged electronics strongly relies on proper cooling. Some type of devices such as IR cooled detectors require cryogenic temperatures on the sensor matrix in order to provide a valuable image feature by low noise to signal ratio.

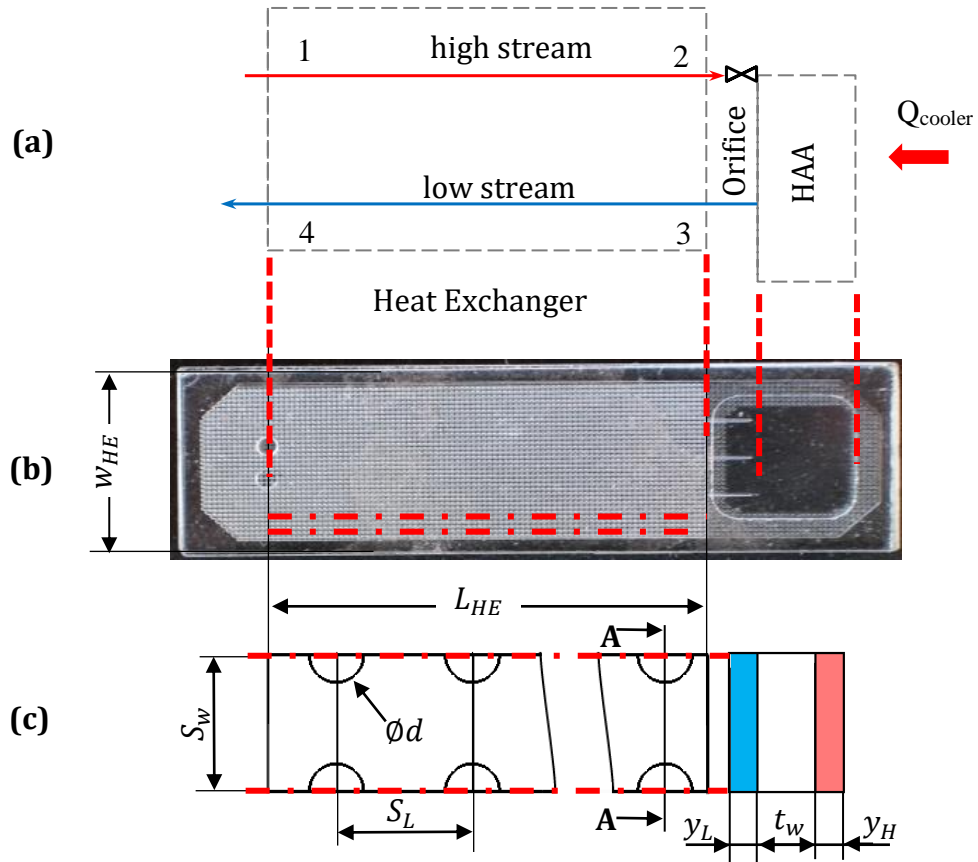


Figure 1 | (a) Schematics of the Joule-Thomson cryocooler. The device has three main parts: counter-flow heat exchanger – used for coolant precooling prior entering the orifice, orifice where isenthalpic expansion (i.e. JT effect) takes place and the heat absorption area (HAA) containing the liquefied nitrogen (in case liquefaction conditions are reached) and absorbing heat from the device that is being cooled. (b) Microscopic image (top-view) of the device; (c) Schematics of the periodic unit cell of the HE channel of total width w_{HE} and length L_{HE} . There are two straight and opposite flow channels one above the other corresponding to the high and low pressure streams, both having the same unit cell width S_w but can have different pin diameter, d , and channel height, y .

One way of cooling to such low temperatures is by using a Joule-Thomson (JT) cooler. The working principle of such a device is the temperature change of a high-pressure gas, when it expands to lower pressure by isenthalpic process, also called throttling process or JT process, [1]. As depicted in **Figure 1** a highly pressurized gas is externally supplied (open loop configuration) to the device at point 1, which is inlet to the high temperature stream of counter flow heat exchanger (CFHE). As the coolant advances toward the high stream outlet, point 2, its temperature decreases due to heat exchange with the low temperature stream. Then, the precooled gas undergoes an isenthalpic expansion through the orifice until it partially liquefies inside the heat absorption area (HAA). The gas conditions inside that section are defined by the saturation state at the inner pressure which is the sum of the pressure losses in line 3-4 and the atmospheric pressure as the outlet (point 4) is opened to the environment. single phase problem, the fluid at gaseous phase enters the low stream of CFHE (point 3) and leaves the device to the atmosphere (point 4) with an increased temperature. Heat interaction with some external source, such as an IR detector, should take place only at the HAA wall with all other walls thermally insulated for reduction of heat losses. From the first law of the thermodynamics the heat interaction equals the specific enthalpy difference between device inlet and outlet multiplied by fluid mass flow rate.

1.2 SETTING THE OPERATING CONDITIONS

The big advantage of this type of cooler is the absence of any moving parts, therefore simplicity, long life span and silent operation. Since the middle of the 20th century a great effort has been invested in making these devices smaller and commercially available. Miniaturization is possible using photolithography manufacturing processes, widely used at semiconductors industry [1]. On the other hand, to achieve considerable cooling effect, i.e. about 80[K] cryogenic temperature, initial conditions prior isenthalpic expansion must be carefully controlled. Some values of a combination of pressure and temperature that are suitable for this purpose are given in **Table B-1** (see Appendix B). We can clearly see that a compromise must be made between the desire to decrease the required working pressure in order to reduce gas supply rate versus the reduction of the heat

exchanger performance in order to make a simpler device. The former results in a smaller difference between the temperature at point 2 and that of point 1. Being guided by pressure levels commonly used in nitrogen operating cryo-coolers, we chose nominal pressure and temperature conditions at point 2 of 2300[psig] and 170[K], respectively.

Table 1 | Summary of boundary conditions at HE's ports, **Figure 1a**.

	Point along the process	Pressure [psig]	Temperature [K]	Remarks
High stream	1	2300	300 [K]	
	2	Based on HE performance	Based on HE performance	Pressure losses can be neglected
Low stream	3	Based on low stream pressure loss	~ 80[K], depends on local pressure	Taken as 80[K] in CFD analysis
	4	0	Based on HE performance	Atmospheric pressure
Mass flow rate = 0 – 2 [SLPM] (38 [mg/s])				Pressure vessel size limited

It can be shown that there is an insignificant high stream pressure loss, thus it is sufficient for the gas supply to provide approximately the same pressure level that is required at point 2. The coolant properties at the boundaries of the HE, which were set accordingly to provided considerations, are given in **Table 1**. In addition, it is logistically convenient to supply a gas at room temperature, hence, necessitating to design a CFHE that can produce a considerable precooling of ~130 degrees. Thus, making the heat exchanger a critical part of every JT cooler design and therefore receiving a special attention in our current study.

1.3 HEAT EXCHANGER DESIGN APPROACHES

A large variety of HE designs were studied throughout the years including macroscale designs, e.g. tube and shell CFHE [2], and more recently miniaturized CFHE designs such as spirals [1], [3], plates stack [4], meandering pipe [1], [3], porous pipe [5] and two straight parallel channels with micro-pins [6].

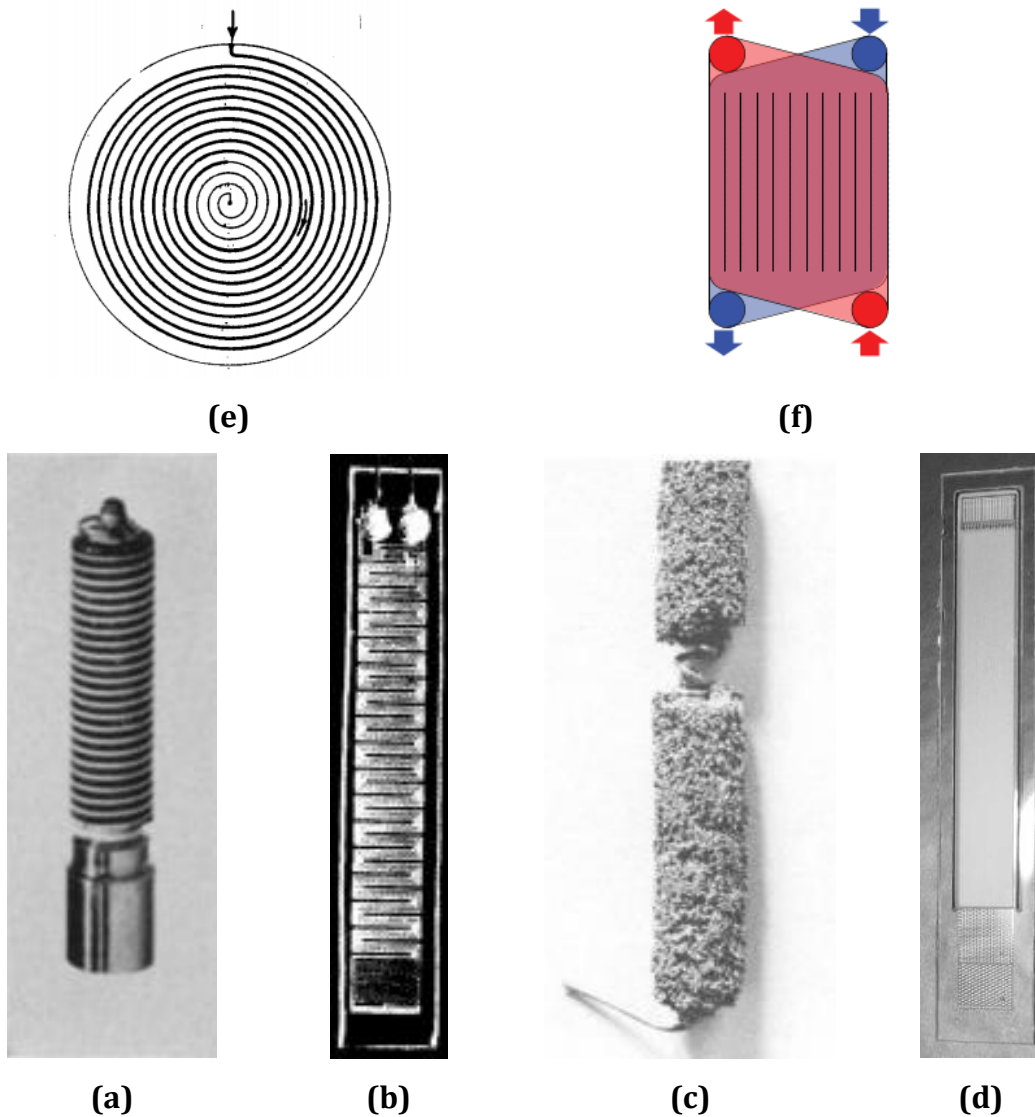


Figure 2 | A variety of heat exchangers configurations studied throughout the years. **(a)** tube and shell, **(b)** meandering pipes, **(c)** porous pipe, **(d)** parallel channels with micro-pins, **(e)** spirals and **(f)** plates stack.

The designs that can be produced using micromachining methods are those depicted in parts b, d, e of **Figure 2** due to their planarity. We chose our heat exchanger's configuration be similar to design (d) since it has the potential to

withstand the high working pressure and can be scaled down for further performance improvement.

1.4 MOTIVATION AND STUDIES OBJECTIVES

Most previous studies used either an experimental approach [1]- [7] with a non-optimized design or performed a numerical investigation of the microscale CFHEs [8] - [9]. Since the cryo-cooler performance depends on many parameters, a method for determining their optimum values should be developed. An earlier attempt based on minimum entropy optimization approach was made in [10].

In the current contribution, we propose a generic procedure for optimizing and verifying, both geometry and mass flow rates of a μ CFHE, operating using nitrogen gas, in order to achieve the highest possible cooling power. We adopt a two straight parallel channels configuration for the high and low temperature streams, both consisting of an array of structural pins. The optimization procedure accounts for the limitation on the pressure drop within the low temperature stream in order to achieve partial coolant liquefaction, and in turn, the JT effect and is supported by CFD analysis and experimental investigation.

2 THEORETICAL METHODOLOGY

2.1 SCALING EFFECTS

Microscale single-phase heat transfer has been intensively studied in the last decades [11]. For single phase heat transfer within microchannel it is generally accepted that the macroscale continuum approach holds for liquids while for gas phase rarefaction effects may occur and this is commonly checked using the Knudsen number, $Kn = \lambda/D_h$, which is the ratio between the mean free path of the fluid molecules to the characteristic length scale of the problem, e.g. the hydraulic diameter D_h . Within the current study the Knudsen number was found to be in the no slip flow regime range, **Table A-1** (see Appendix A), in order of 10^{-6} and 10^{-4} for the high and low streams, respectively.

Another issue that needs consideration is the possible compressibility effects as checked using the Mach number $Ma = V/a$, wherein V is flow speed and a is speed of sound, and was found to be smaller than 0.3, thus, suggesting incompressible flow conditions [12]. In the current study the resulting Mach number was 0.08 at the low-pressure stream and two orders of magnitude lower at the high-pressure stream. However, this criterion is a necessary but not a sufficient condition for considering the flow as being incompressible. Due to significant density variations as a result of both large temperature and large pressure variations these effects were taken in account in the CFD analysis, while neglected in calculations based on empirical and analytical correlations.

The importance of the varying temperature dependent fluid properties, e.g. viscosity and thermal conductivity, on flows within micro-sized channels was validated by [13], reporting increase of about 30[%] in Nu for temperature dependent fluid properties comparing to the solution with using only constant values. In the current study, we used both solution based on empirical correlations utilizing averaged nitrogen properties and more precise numerical simulations (ANSYS Fluent software) incorporating real gas model with nitrogen properties depending on local pressure and temperature. Comparing results obtained using the real gas model to those obtained using average fluid properties, indicates a 10[%]

error in the T_2 value as calculated using CFD. This finding explains the temperature error produced by approximate solution, when comparing it to CFD analysis results, **Table 3**.

In micro heat exchangers (μ HT) the axial conduction within the separating solid wall may strongly influence the heat patterns (conjugate heat transfer) particularly at low Re and should be accounted for. This is checked using the Maranzana number, $M = \left(\frac{t_w}{L_{HE}} \right)^2 \frac{NTU}{Bi}$, which is the ratio between the axial heat conduction within the solid walls of the channel and the heat transfer by convection within the fluid [14]. Herein, $Bi = \frac{ht_w}{k_w}$, t_w and k_w , are the separating wall thickness and thermal conductivity, L_{HE} is the heat exchanger length, NTU is defined by EQ. (13) and h is convective heat transfer coefficient. For the current test study conditions the Maranzana number was found to be sufficiently small (~ 0.003 and 0.002 for the low and high streams, respectively, relative to the criteria of 0.01) to justify negation of axial conduction effects in the approximate solution based on empirical correlations, while in the CFD analysis the heat conduction within the separating wall is inherently accounted for.

Numerical investigation [15] of the effect of separating wall thermal conductivity on μ CFHX effectiveness indicates that optimal HE performance is achieved for thermal conductivity value of about ~ 1 [$\text{Wm}^{-1}\text{K}^{-1}$], **Figure A-1** (see Appendix A), which is true for borosilicate glass and some other ceramic materials. We used Schott D 263® T ECO glass with a value of about 1.2 [$\text{Wm}^{-1}\text{K}^{-1}$] as provided by the manufacturer [16], **Table B-2** (see Appendix B).

2.2 CORRELATIONS FOR HEAT TRANSFER COEFFICIENT AND PRESSURE DROP

Both CFHE streams were chosen to consist of a single straight channel with uniformly spaced pins (**Figure 1c**). These pins have two roles: supporting the channel structure to withstand high fluid pressure, see Appendix E, and enhancing local Reynolds number due to mixing, thus, improving internal convective heat transfer coefficient. Pressure losses inside the channel were approximated by superposition of two contributions – the first is due to flow across the infinite long

cylindrical pins (in absence of more appropriate correlation), while the second is due to the channel walls.

For the first, we used a well-known correlation, which was empirically derived for a case of fluid flow across tube banks, given by

$$\Delta p_{pins} = N_L \left(\frac{\rho V_{max}^2}{2} \right) f^* \quad , \quad (1)$$

here V_{max} is the averaged fluid velocity in narrowest cross-section, see section A-A

Figure 1c, N_L is the number of pins in the flow direction, ρ is the free stream average density and f^* is the empirical factor for inline pins arrangement [17]

$$f^* = \left[0.044 + \frac{0.08 S_L / d}{[(S_w - d)/d]^{0.43} + 1.13 d / S_L} \right] Re_{max}^{-0.15} \quad (2)$$

where in case of a uniform pin spacing, $S_w = S_L$ (**Figure 1c**), d is pin diameter and Re_{max} is evaluated at V_{max} , with the pin diameter as the reference length scale. The Re_{max} value, calculated using the averaged coolant properties, for the high and low pressure streams is about 310 and 630, respectively, at optimum mass flow rate of 22.5[mg/s] (see Section 3.3).

The pin spacing for isotropic wet-etching micromachining technique is related to the channel depth, y

$$S_w = d + 2y + 50[\mu m] \quad (3)$$

where the minimum feature in the mask is 50[μm] due to the resolution limitation. For the second pressure loss mechanism, we used the relation for the pressure loss within a channel flow [18]

$$\Delta p_{wall} = \frac{1}{2} \rho V^2 f \frac{L_{HE}}{D_h} \quad (4)$$

where V is the full channel cross-sectional (i.e. without accounting for the pins) averaged fluid velocity, L_{HE} is the HE length, $D_h = 2y$ is the hydraulic diameter and $f = 96/Re_D$ is the friction factor [19], **Table A-2** (see Appendix A), when Re_D using hydraulic diameter as length scale.

Thus, the overall pressure loss within the channel with pins is

$$\Delta p_{channel} = \Delta p_{pins} + \Delta p_{wall} \quad . \quad (5)$$

Pressure loss calculations, using averaged values of coolant density and viscosity, found producing relatively high errors, about 30[%]. In this work, we used an iterative method of correcting their values, accordingly to temperature profile along the HE. This profile was achieved by solving an energy balance differential equations for both streams simultaneously, the NTU method, presented in details in Appendix D.

Heat transfer calculations involved an estimation of the channel convective heat transfer coefficient within each of the streams. We adopted the following experimentally derived correlations [20]

$$Nu = 0.069 \cdot Re_{max}^{0.728} @ \frac{S_w}{d} = 2.5 \quad (6)$$

and

$$Nu = 0.092 \cdot Re_{max}^{0.707} @ \frac{S_w}{d} = 1.5 \quad (7)$$

where for intermediate S_w/d values, Nu was interpolated between EQs. (6) and (7). The average Nusselt number is evaluated using the pin diameter as the reference length scale. The matching convective heat transfer coefficient, for each stream, is evaluated using following definition and average nitrogen thermal conductivity

$$h = \frac{kNu}{d} \quad . \quad (8)$$

2.3 HEAT EXCHANGER AND COOLER EFFECTIVENESS RELATIONS

The HE effectiveness is defined as the ratio of the actual heat transfer rate for the heat exchanger to the maximum possible heat transfer rate. The latter is calculated for the stream wherein the fluid has the minimum heat capacity rate $C_{min} = \min(C_L, C_H) = \min(\dot{m}Cp_L, \dot{m}Cp_H)$ hence experiencing the maximum possible temperature difference. Herein Cp is the specific heat and the subscripts H and L refer to the high and low streams [18].

In our device, the gas in the low temperature stream always has the lowest specific heat and therefore also the minimum heat capacity rate since both streams have the same mass flow rate. Hence, for equal mass flow rates, the heat exchanger effectiveness is given by

$$\epsilon_{HE} = \frac{\Delta i_{34}}{\Delta i_{34 \max}} = \frac{i_4 - i_3}{i_{4 \max} - i_3} \quad , \quad (9)$$

where the maximum possible enthalpy value at point 4, $i_{4 \max}$, will be reached if HE low stream exit temperature reaches the high stream inlet temperature, i.e. in a case $T_{4 \max} = T_1$. The enthalpy at point 3, i_3 – is taken as saturation value for vapor phase, at 80[K] temperature. Using same definition, we can define the cooler effectiveness as

$$\epsilon_{cooler} = \frac{\Delta i_{14}}{\Delta i_{14 \max}} = \frac{i_4 - i_1}{i_{4 \max} - i_1} \quad . \quad (10)$$

By eliminating i_4 using EQ. (9) one obtains the cooler effectiveness as a function of HE's and nitrogen known properties

$$\epsilon_{cooler} = \epsilon_{HE} + (1 - \epsilon_{HE}) \frac{i_1 - i_3}{i_1 - i_{4 \max}} \quad . \quad (11)$$

The resulting linear curve, **Figure 3**, calculated for constant high stream inlet properties, shows strong dependency of cooler performance on that of the HE and poses very strict requirement regarding the heat exchanger performance.

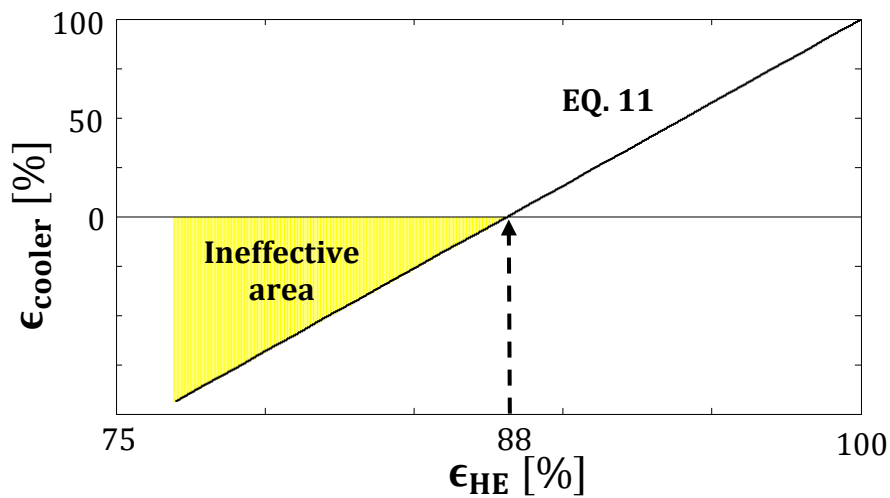


Figure 3 | Cooler effectiveness dependency on heat exchanger effectiveness for constant inlet conditions. It is noted that for HE effectiveness values below 88[%] saturation conditions cannot be reached.

Essentially, in order to produce considerable cooling, HE effectiveness value should be above 88[%], otherwise desired effect isn't achievable at all.

For CFHE with negligible axial conduction within the separating wall, a closed-form analytical solution is obtained by the NTU method, [21]

$$\epsilon_{HE} = \frac{1 - e^{-NTU(1-C)}}{1 - Ce^{-NTU(1-C)}} \quad (12)$$

where for the case of streams with equal mass flow rate, $C = Cp_{34}/Cp_{12}$ (averaged values are used) and NTU non-dimensional number, is defined as

$$NTU = \frac{U_{tot}A_{wall}}{Cp_{34}\dot{m}} \quad , \quad (13)$$

where A_{wall} is pins free wall area in flow transverse direction (i.e. projected pin total area subtracted from the microchannel total cross-sectional area), \dot{m} is nitrogen mass flow rate and U_{tot} denotes total heat transfer coefficient, which is given by the series connection of the thermal resistors in the flow transverse direction

$$U_{tot} = \frac{1}{\frac{t_w}{k_w} + \frac{1}{h_{12}} + \frac{1}{h_{34}}} \quad , \quad (14)$$

where h_{12} and h_{34} are high and low stream inner heat convection coefficients, respectively, calculated by EQ. (8). Finally, using first law of thermodynamics the micro-cooler cooling power of a perfectly insulated HE, also called gross cooling power, is defined by

$$\dot{Q}_{cooler} = \epsilon_{cooler} \dot{m}(i_1 - i_{4max}) \quad . \quad (15)$$

This is the most important relation in the cooler design, which will serve us in the optimization stage, and as will be shown later, this cooling power is the heat rate required to fully evaporate the condensed nitrogen within the HAA.

3 OPTIMIZATION METHODOLOGY

3.1 OPTIMIZATION NEED JUSTIFICATION

A list of all parameters appearing in the above equations, their values and effect on the cooler performance are given in **Table A-3** (see Appendix A). In addition, a summary of the nitrogen properties at the HE ports is given in **Table 1**. These parameters play a role in the parametric optimization process and the known boundary values leaves five free parameters (\dot{m} , y_H , d_H , y_L , d_L) to play with.

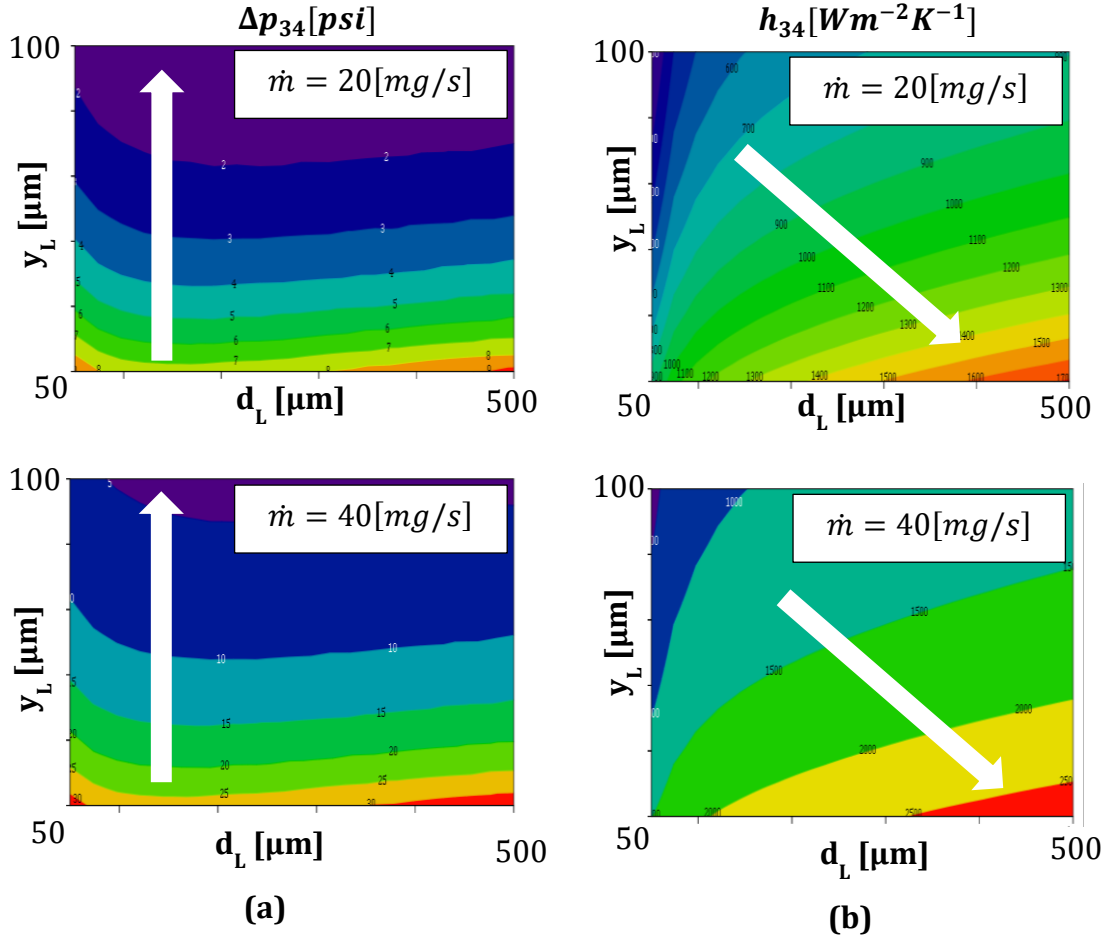


Figure 4 | Trends of parameters behavior for achieving desired problem quantities, at low pressure and temperature stream. **(a)** Pressure losses map, plotted for variable values of channel height, y_L , pin diameter, d_L , and coolant mass flow rate, \dot{m} . Lower (desirable) values are obtained for largest channel height and smallest mass flow rates; **(b)** Convection heat transfer coefficient map, plotted for the same variable parameters. Higher (desirable) values are obtained for smallest channel height and largest mass flow rates.

To prove that indeed we have an optimization problem, plots of the pressure losses and convection heat transfer coefficient for the low stream of the CFHE are given in **Figure 4a** and **b**, respectively. The former is important since HAA wall temperature is governed by the local pressure, as saturation conditions requires, and thus depends on low stream pressure drop. By using the saturation properties of nitrogen gas the temperature rise as a result of pressure loss between points 3 and 4 can be approximated to be as up to 4[K] beyond the desired temperature value of 80[K], when pressure loss is varied in range of 5-15[psi]. IR detector performance is heavily affected by the temperature of its sensing matrix, therefore, we posed a limitation on the maximum pressure drop value of 10[psi]. The goal is to achieve higher precooling, i.e. better heat interaction inside the HE, hence, we need to maximize the overall heat transfer coefficient. According to EQ. (14) this can be achieved by maximizing each of the stream's heat transfer coefficients and reducing the wall thermal conduction resistance. Part of design process is choosing right values of the free parameters so that both desired trends will occur, i.e. minimizing the pressure drop and maximizing heat transfer rate. However, close examination of the plots in **Figure 4** reveals a contradictive behavior thereby justifying problem optimization. The overall behavior of the high stream heat transfer coefficient is similar besides the insignificant pressure drop, which was found to be ~ 0.15 [psi] at the given conditions using both, pressure loss approximation, EQ. 5, and CFD analysis

3.2 OPTIMIZATION SCHEME

The optimization procedure goal is maximizing the cooling power under the limitation of the low stream pressure drop. An optimization function incorporating both effects is proposed as following

$$f_{opt}(d_H, d_L, y_H, y_L, \dot{m}_f) = (\dot{Q}_{cooler} - \dot{Q}_T)^2 + 10(\Delta p_{34} - \Delta p_T)^2 \quad (16)$$

where \dot{Q}_{cooler} defined by EQ. (15), Δp_{34} is the low stream pressure loss from EQ. (5), while the target values for the cooling power and pressure drop were set to $\dot{Q}_T = 5[W]$ and $\Delta p_T = 10[psi]$, respectively. It should be noted that the exact form of the optimization function is quite arbitrary since the optimization is robust

enough if both effects are accounted for, as tested by examining various forms, but may need some tuning.

A minimization operator was applied on the optimization function EQ. (16), using PTC Mathcad software, built in “minimize” function, incorporating Conjugate Gradient method, for smoothing non-linear optimization [22], while all geometrical parameters could vary in range of 50 – 500[μm] and the maximum mass flow rate was set to 40[mg/s]. In order to simplify the HE solution we forced both high and low channels to consist of a periodic unit cell of the same width, S_w (EQ. 3), adding a constrain of the form

$$d_H + 2y_H = d_L + 2y_L \quad . \quad (17)$$

3.3 OPTIMIZATION RESULTS

The resulting optimum geometry, mass flow rate and approximated cooler performances using these values, are given in **Table 2**.

Table 2 | Results of the optimization procedure obtained using the approximate solution.

Optimization Results	Approximated cooler performance
$y_H = 50[\mu\text{m}]$	$Q_{cooler} \sim 360[\text{mW}]$
$y_L = 50[\mu\text{m}]$	$\Delta p_{3-4} \sim 10[\text{psi}]$
$d_H = 100[\mu\text{m}]$	$T_3 \sim 82[\text{K}]$
$d_L = 100[\mu\text{m}]$	$\epsilon_{HE} \sim 95[\%]$
$\dot{m} = 22.5[\text{mg/s}]$	$\epsilon_{cooler} \sim 50[\%]$

It is seen that the optimization procedure results in identical geometry for both HE streams. This result can be intuitively explained from EQ. (13) by noting that the heat transfers rate scales with A_{wall} , a relation that assumes that the heat transfer between the HE streams takes place only through the common area that is free of pins, thus, resulting in an identical pin geometry on both of the separating wall sides. However, it should also be noted that the resulting optimal pin diameter is not at its lower value, namely, the resulting separate wall area is not a maximum one due to the contradictive trend of convective heat transfer coefficient enhancement due to

the presence of the pins. To further support the optimization results based on the empirical correlations we turned to the aid of a finite element numerical solution.

4 CFD ANALYSIS METHODOLOGY

4.1 COMPUTATIONAL MODEL

A simplified parametric model of the heat exchanger was constructed in Workbench Modeler® and meshed by Fluent® module.

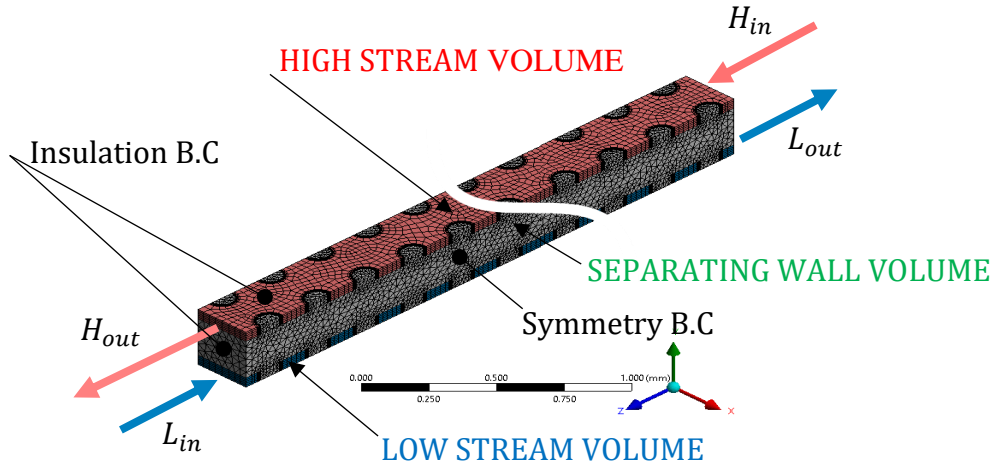


Figure 5 | Computational model of the periodic unit cell simulated in Fluent and consisting of the high and low fluid streams and the separating wall. Surfaces pointing in the directions Z and Y are thermally insulated due to the low thermal conductivity of the contacting glass which is omitted from the model while the surfaces pointing in the direction X obeys symmetry conditions.

Boundary walls conditions and nitrogen properties at the heat exchanger ports are given in **Figure 5** and **Table 1**, respectively. The fluid domain was meshed using CFD physics preferences enhanced by using of fine sweep meshing with fully controlled elements distribution in the flow and transverse directions. To achieve the required mesh resolution at the fluid-solid interface, especially around the cylindrical pins, curvature based sizing function was enabled and near walls mesh inflation was added. The mesh constructed using preferable hexahedron elements for the fluid domain and highly location adapted, tetrahedron elements for the solid, resulting in mesh with over one million (1M) elements having superior mean orthogonal quality of 0.87 (out of 1.0). Additional mesh resolutions of 500K and 1.5M elements were tested, confirming that selected mesh resolution (1M) is appropriate for solving given problem. Momentum equation, corrected by $k-\epsilon$

turbulent model, [23] , and enhanced wall treatment, along with the continuity and energy equations were successfully solved at steady-state conditions using a coupled scheme, [23].

The above coupled heat transfer and fluid flow problem is characterized by a relatively low Reynolds number, yet attempting to solve it at steady state and laminar flow conditions was unsuccessful, as the governing equations (energy, momentum and continuity) failed to converge. There may be two reasons for this, first, early transition to turbulence [24], and second, vortex shedding effect which necessitates a time-dependent solution [25].

4.2 MODEL VALIDATION

Comparing the CFD analysis results of the heat exchanger model at nominal working point with the approximate solution based on empirical correlations results in about 15[%] relative error in low stream pressure loss estimation and less than 1[%] in heat exchanger effectiveness, **Table 3**.

Table 3 | CFD solution verification by compare against approximate solution basing on experimental and analytical correlations.

Quantity	Approx. solution	CFD	Relative error [%]
$T_2[K]$	142.1	161.0	11.75
$T_4[K]$	286.5	288.9	0.8
$U_{tot}[Wm^{-2}K^{-1}]$	1060	967.1	9.9
$\Delta p_{12}[psi]$	0.16	0.15	4.0
$\Delta p_{34}[psi]$	10.9	12.7	14.2
$\epsilon_{HE}[\%]$	96.7	97.3	0.6

These relatively small errors, mainly due to the averaged nitrogen properties used by the approximate solution, suggesting that a meaningful solution was achieved, therefore, validating the computational model.

4.3 VERIFICATION OF OPTIMUM GEOMETRY AND MASS FLOW RATE

After successful validation of the CFD analysis and HE model the main objective became the verification of the optimization procedure results. For this purpose, we performed a parametric analysis using the computational model discussed above, i.e. parametric variation and investigation of the heat exchanger performance. First, the approximated optimal geometry was validated by varying the channel geometry while keeping the mass flow rate constant, **Table 4**. Then, the micro-cooler cooling power dependency on the mass flow rate was studied. From EQ. (15) one may conclude that the cooling power should monotonically rise with increasing mass flow rate. However, this increase is also affecting the HE effectiveness in an opposite way since the NTU is decreasing as a result. The general behavior cannot be easily seen without calculating the cooling power dependency on the mass flow rate, **Table 4**, from which one concludes that the selected mass flow rate is both optimal and robust since its variation doesn't affect much the resulting cooling power.

Table 4 | Verification of optimization results by CFD analysis

	Geometry verification		
	Optimum design	Design 1	Design 2
	$S_w = 250[\mu m]$ $d_{H,L} = 100[\mu m]$ $y_{H,L} = 50[\mu m]$	S_w - optimum d_H, y_H - optimum $d_L = 50[\mu m]$ $y_L = 75[\mu m]$	$S_w = 350[\mu m]$ $d_H = 200[\mu m]$ $y_H = 50[\mu m]$ $d_L = 100[\mu m]$ $y_L = 100[\mu m]$
$\epsilon_{HE} [\%]$	83.1	81.9	73.3
	Mass flow rate		
	20 [mg/s] (optimum - 10[%])	22.5 [mg/s] (optimum)	25 [mg/s] (optimum +10[%])
$Q_{cooler} [mW]$	355	361.3	361

In the above analysis, we targeted at achieving a saturation condition at the HAA and assumed a pure nitrogen gaseous phase at point 3. The latter necessitates the absorption of heat in order to increase the nitrogen quality to 100[%] and it should correspond exactly to the cooling power, EQ. 15. This is verified, using CFD, by examining at the optimum geometry and mass flow rate conditions, that the nitrogen quality immediately following the isenthalpic expansion is ~ 90 [%], which fits the cooler power reported in **Table 4**.

As last step of the verification process, the parasitic effect of the axial heat conduction within the separating wall on the HE effectiveness was studied in order to verify the conclusion derived by [15], **Figure A-1** (see Appendix A), regarding selection of material for μ HE structure. We used the optimal geometry and mass flow rate in our analysis and only varied the wall thermal conductivity. The resulting HE effectiveness (**Figure 6**) indicates good agreement with the conclusion of [15] and material used for constructing the cooler prototype, **Table B-2** (see Appendix B).

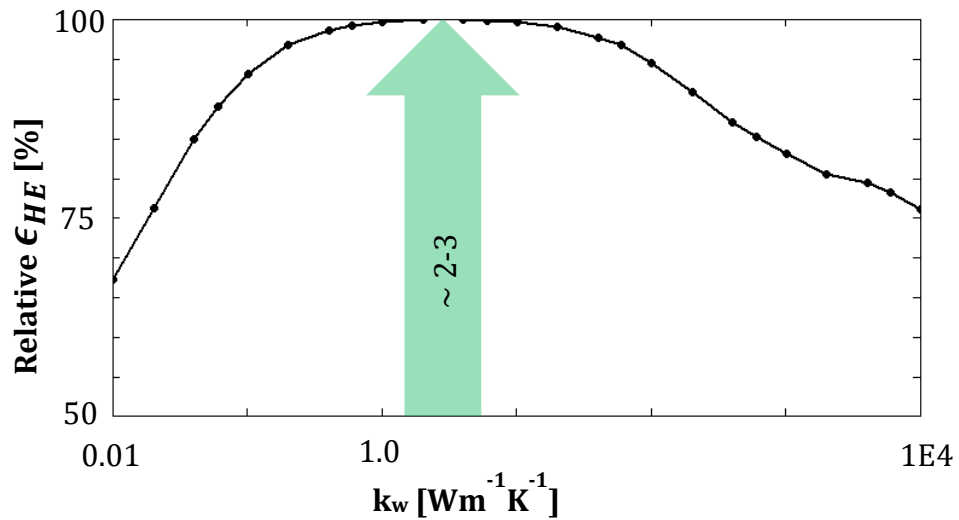


Figure 6 | Relative effectiveness dependency on the separating wall thermal conductivity. Maximum performance is achieved for thermal conductivity of $\sim 2-3$ [$\text{Wm}^{-1}\text{K}^{-1}$] and in agreement with previous studies [15].

5 EXPERIMENTAL METHODOLOGY

5.1 CHIP DESIGN AND FABRICATION

Standard photolithography and etching techniques were used for the chip fabrication. The channel made of Schott D 263® T ECO glass was fabricated using wet etching process with Hydrofluoric acid. The etching process was adapted for that specific glass in order to produce circular pins with controlled diameter and height and without defects, Figure F-1 | (see Appendix F). In order to compensate for over-etching, which is typical of the wet etching process, we used a protective coating made of 2000[Å] gold and 200[Å] chromium layers, with an opening window having a minimum width of 50[μm]. Three glass wafers were used to produce one cooler assembly, **Error! Reference source not found.** (see Appendix F), where the top and bottom slides, having a thickness of 0.55[mm], consisted of the channels with an identical pins pattern. In the top slide, which is part of high pressure stream, additional channels were etched, to serve as orifices. The intermediate piece was used as the separating wall between the streams having thickness of 0.21[mm]. The smaller thickness was chosen to improve both transverse heat transfers and axial heat losses. In the intermediate and bottom parts, rectangular openings were etched, to enable the coolant passage from the orifice in the high stream channel to the low stream channel and to produce a cavity for the HAA section. All pieces were structurally connected and sealed using the thermal bonding process [26] that was adjusted for our use and materials of choice.

5.2 TEST BENCH DESIGN

The experiments were conducted in a test setup (**Figure 7**) specially designed for the testing of glass made microcooler prototypes.

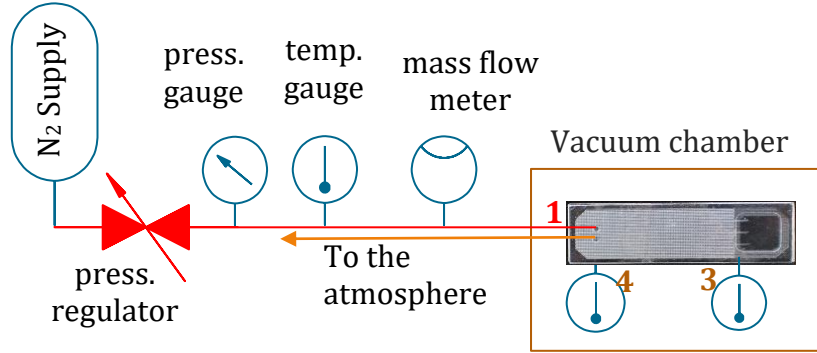


Figure 7 | Schematics of the experimental setup. The coolant is supplied from a N₂ vessel and its pressure controlled using a pressure regulator that is assembled on the supply line before the device inlet (point 1) along with pressure, temperature and mass flow rate gauges. To reduce the heat interaction of the device with the environment the entire device was under vacuum and fixed by a special holder which also have role of an inlet and outlet manifold. In addition, temperature measurements point 3 and 4 were obtained using externally (to the glass) bonded thermocouples.

Pressurized nitrogen at room temperature was supplied to the cooler which was thermally insulated from the surrounding by using air free environment, vacuum level of about 30[mbar], and a fixture made of low thermally conductive stainless steel. Supplied pressure was reduced to the desired level with a pressure regulator. Gas inlet conditions: pressure, temperature and flow rate, were measured by specialized and calibrated flow meter. Two type K thermocouples were attached to the bottom surface of the cooler, one at the HAA outer surface (point 3) and another at the device outlet (point 4). The temperatures T_3 and T_4 within the device were estimated from these externally measured temperatures using a heat flux balance between the heat lost to the environment by radiation (EQ. 18) and the heat supplied by convection and conduction (EQ. 19) through the wall.

$$q''_{rad} = \epsilon \sigma_b (T_w^4 - T_{env}^4), \quad (18)$$

where glass emissivity, $\epsilon \cong 0.8$, σ_b – is Stefan-Boltzmann constant, T_w and T_{env} , are wall (measured) and the environment (room) temperatures.

$$q''_{bulk} = \frac{1}{\frac{t_{w_ext}}{k_w} + \frac{1}{h_{34}}} (T_{bulk} - T_w) \quad (19)$$

here external wall thickness - $t_{w_ext} = 0.55[mm]$ and T_{bulk} is nitrogen temperature at points T_3 or T_4 .

6 RESULTS AND DISCUSSION

During the tests the inlet pressure rose gradually causing a corresponding variation in the mass flow rate. The change in the inlet conditions was followed by variation of temperatures measured at points 3 and 4 (see **Figure 7**). In order to reach steady state conditions, the device was left to run about 5[min] at constant inlet conditions until all temperature gauges reached steady reading and then the data was recorded. Several experiments were conducted with inlet pressure in the range of 54 to 398 [psig] and corresponding mass flow rates of 3 to 30 [mg/s] (see **Table 5**, for a detailed list of all experiments). For these values of the inlet pressure cryogenic temperatures cannot be achieved, therefore, we forced temperature at the low stream inlet in the CFD model to be equal to T_3 measured in the experiments, in order to obtain comparable data of HE problem solution.

Table 5 | Detailed listing of experiments conducted on first prototype.

Test No.	Input parameters			Measured temperatures	
	$p_1[psig]$	$\dot{m}[mg/s]$	$T_1[C]$	$T_3[C]$	$T_4[C]$
1	54	3.05	20.5	19.1	20.3
2	97	6.49		17.4	20.1
3	150	10.5		14.7	19.8
4	191	13.74		12.5	19.4
5	223	16.22		10	18.7
6	273	20.04		6.3	17.7
7	306	22.71		3.8	16.9
8	333	24.62		1.8	16.2
9	358	26.72		-0.1	15.5
10	380	28.44		-1.9	14.9
11	398	29.97		-3.3	14.5

We performed a series of CFD simulations with boundary conditions identical to the experiments with the goal of estimating the error produced by the proposed numerical method. But first, our computational model deviation from the actual device must be understood. In reality, after passing the HE, the gas expands in the orifice and enters directly to the cold stream side of the CFHE. In the model, where only the HE part of the microcooler is resolved, the heat exchanger streams are separated, therefore must be compensated for the missing boundary conditions at the inlet of the low stream by using forced values which are corrected accordingly to performed tests. Second source of disparity between the model and prototype is the perfect thermal insulation assumption which is implemented in the computational model. Our experimental setup was designed to provide reduction in heat losses due to the natural convection heat transfer, but it provides no shielding from the radiation mechanism, so we need to estimate these losses in order to obtain valid results. The last major difference between our model and the actual device are the thermally insulated boundary conditions applied on the external edges of the separating wall in the CFD model.

First, the value of temperature difference between the HAA wall and the device inlet which defines the device maximum temperature drop and referred here as cooling effect was studied (**Figure 8a**). There are two cooling mechanisms that act in series on the high temperature stream of the HE that contribute to this effect: heat exchange with the low temperature stream followed by JT isenthalpic expansion in the orifice section. The overall measured temperature decrease between points 1 and 3 was only 1.4[°C] in the experiment conducted with the lowest inlet pressure magnitude and reached a level of 23.8[°C] at the maximum pressure level. The contribution of the HE to the total temperature decrease was about 0.6[°C], which is 43.6[%], at the lowest tested pressure and reached a maximum of 17.4[°C], about 73[%], at experiments with the highest available pressure.

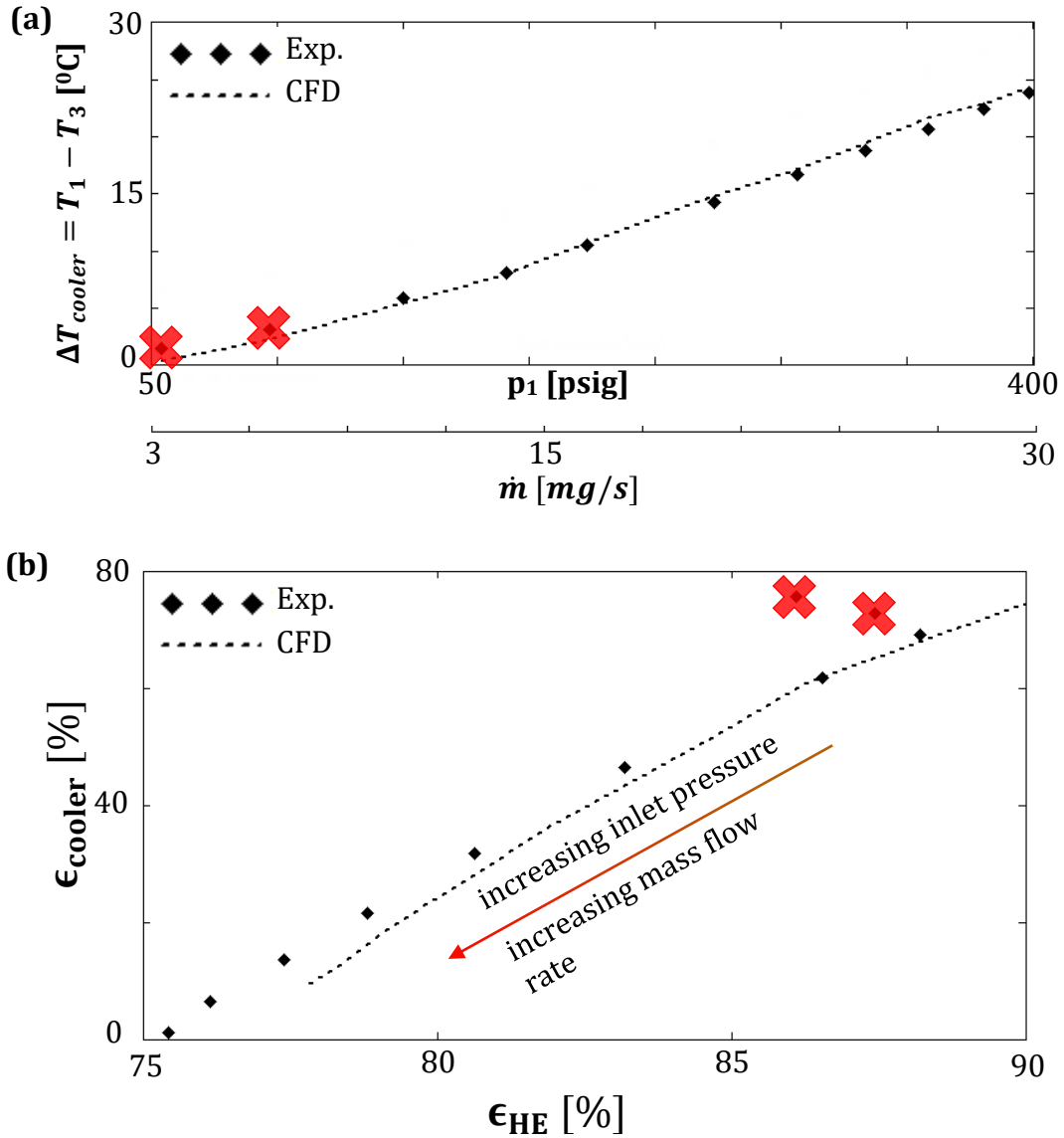


Figure 8 | Comparison of the CFD and experimental results. **(a)** Cooling effect achieved in the experiments, defined by the temperature difference between the inlet and heat absorption area wall, versus the inlet pressure. It is noted that the cooling effect is increasing with increasing inlet pressure. The error range presented is ± 1 [°C], which is maximum estimated absolute error between the experimental data and numerical simulation. The two points marked by red crosses represent experiments where ideal insulation assumption has been violated. **(b)** Cooler effectiveness dependence on HE effectiveness, where every point stands for a different experiment. This, nonlinear behavior, differs from one presented in **Figure 3**, since each experiment has a new set of inlet conditions. CFD analysis results lie in the 3 [%] maximum absolute error range from the experimental data excluding two points marked by big red crosses, presenting experiments where ideal insulation assumption is violated.

It can be seen, that at the tested pressure levels, the heat exchange inside the CFHE is the dominant cooling mechanism, so by comparing the overall cooling effect, we can tell with high confidence level how good our model, which have only the HE section, predicts the cooler performance. Comparing experimental results to numerical analysis, resulted in absolute error of less than 1[°C] for all valid points, when temperature T_3 in numerical data calculated from T_2 , which obtained directly from the CFD analysis, by using isenthalpic expansion process which taking place between points 2 and 3, with estimated orifice efficiency of 98[%]. Two first points of experimental data, total 11 were measured, corresponding to slow flow rates of 3 and 6.5 [mg/s], were found to violate the perfect insulation assumption and were disqualified for further use. At these points the estimated radiation heat transfer, from the “hot” environment to the low stream of the HE, was found to be more than 40[%] of the total heat received by this stream, resulting in corresponding heat unbalance between HE streams (see Appendix C, for heat radiation losses calculation scheme).

The importance of heat exchanger effectiveness has already been discussed in previous sections, where it was shown that knowing this parameter enables us to tell how good our device will perform as a cooler, by using EQs. (11), (15) and gas conditions at the inlet. Values calculated from the experimental data were compared against Fluent analysis results, **Figure 8b**. We can see that for both data sets, the heat exchanger effectiveness is decreasing as mass flow rate increasing, as should be expected from definition of NTU – EQ. (13) and ϵ_{HE} – EQ. (12). The inlet conditions were varied in each test, therefore overall behavior is not linear, as predicted by EQ. (11), but both data sources are producing a similar trend. The mean absolute difference between the experimental data and Fluent results was about 3[%], when numerical simulation consistently underestimates the cooler effectiveness. Since the results of first two experiments were disqualified, for the rest of data points maximum achieved cooler effectiveness was about 70[%] corresponding to HE effectiveness of 88[%].

7 CONCLUSIONS AND FUTURE WORK

We managed to utilize known empirical correlations for the flow and heat transfer problem in macroscale devices for optimization of microscale CFHE integrated within a JT cryo-cooler device. The correlations were used for obtaining an approximate optimum solution which was then validated using the more accurate but laborious CFD analysis. It was concluded that the optimum geometry and mass flow rate obtained from the approximate solution is very useful for initial design stages as it is capable of resolving the pressure loss and HE's effectiveness with accuracy of 15[%] and 1[%], respectively.

A glass made microcooler prototype, having an optimum geometry, was built using photolithography and thermal bonding micromachining techniques. Fortunately, the glass was found to be an almost ideal structural material since its thermal conductivity, as indicated by previous studies and current numerical simulations, led to an optimized suppression of axial conduction on one hand and enhanced heat transfer between the high and low temperature streams on the other hand. The experimental data and numerical simulations resulted in good agreement of $\sim 1[^\circ\text{C}]$ difference, suggesting that the CFD simulation can adequately resolve flow and heat transfer in JT micro-cooler. In addition to above conclusion, the device thermal insulation must be properly designed in order to achieve considerable cooling effect. Thus, our study verifies the proposed optimization technique for performance enhancement of micro JT cryo-cooler having uniformly spaced structural pins. Due to its generality, the optimization approach is applicable for various heat exchanger designs.

Unfortunately, we could not demonstrate coolant liquefaction due to limitation on maximum allowable inlet pressure of about 400[psig], that the current device can withstand without breaking. In order to reach ~ 2300 [psig] required for liquefaction, without cooler's structure failure, other structural improvements are necessary including the possible use of other than glass fabrication technology such as Lithography-based Ceramic Manufacturing (LCM) which is currently studied by us. This type of additive manufacturing technology, is capable of producing complex structures, with relatively high resolution, and made of high strength and low conductivity ceramics. This technology's limitation in terms of its resolution,

uncured material removal and resulting material thermal and mechanical properties, requires further study.

8 REFERENCES

- [1] W. A. Little, "Microminiature refrigeration," *Review of Scientific Instruments* 55.5, pp. 661-680, 1984.
- [2] S. W. Stephens, "Advanced design of Joule-Thomson coolers for infra-red detectors," *Infrared Physics* 8.1, pp. 25-35, 1968.
- [3] E. Mikulin, Y. Shevich, T. Danilenko, N. Solovov and V. Veselov, "The miniature Joule-Thomson refrigerator," *Cryogenics* 32, pp. 17-19, 1992.
- [4] Y. Yang, G. L. Morini and J. J. Brandner, "THE DESIGN OF GAS-TO-GAS MICRO HEAT EXCHANGERS," *Engineer & the Machinery Magazine*, vol. 54, no. 644, pp. 69-92, 2013.
- [5] M. Chorowski, E. Bodio and M. Wilczek, "Development and testing of a miniature Joule-Thomson refrigerator with sintered powder heat exchanger," *Advances in cryogenic engineering*, pp. 1475-1481, 1994.
- [6] Lerou, P.P.P.M., et al., "All-Micromachined Joule-Thomson cold stage," pp. 437-441, 2007.
- [7] H. J. e. a. Holland, "Miniature 10–150mW Linde-Hampson cooler with glass-tube heat exchanger operating with nitrogen," *Cryogenics* , vol. 38.4, pp. 407-410, 1998.
- [8] J. Sangkwon, "How difficult is it to make a micro refrigerator," *International Journal of Refrigeration*, vol. 27.3, pp. 309-313, 2004.
- [9] Y.-J. e. a. Hong, "A numerical study of the performance of a heat exchanger for a miniature Joule–Thomson refrigerator," *Cryocoolers*, vol. 15, pp. 379-386, 2009.
- [10] Lerou, P. P. P. M., et al., "Optimization of counterflow heat exchanger geometry through minimization of entropy generation," *Cryogenics*, vol. 45.10, pp. 659-669, 2005.
- [11] P. Rosa, T. G. Karyiannis and M. W. Collins, "Single-phase heat transfer in microchannels: The importance of scaling effects," *Applied Thermal Engineering*, vol. 29, pp. 3447-3468, 2009.
- [12] J. D. Anderson Jr., *Modern Compressible Flow*, New York: McGraw-Hill, 2003.
- [13] H. Herwing and S. P. Mahikular, "Variable property effects in single-phase incompressible flows through microchannels," *International Journal of Thermal Sciences*, vol. 45, pp. 977-981, 2006.

- [14] G. Maranzana, I. Perry and D. Maillet, "Mini- and micro-channels: influence of axial conduction in the walls," *Int. J. of Heat Mass Transfer*, vol. 47, pp. 3993-4004, 2004.
- [15] T. Stief, K. Schubert and O.-U. Langer, "Numerical investigation of optimal heat conductivity in micro heat exchangers," *Chem. Eng. Technol.*, vol. 21, pp. 297-303, 1999.
- [16] Schott, "Schott - Advanced optics," 24 April 2016. [Online]. Available: www.schott.com.
- [17] M. Jakob, "Heat Transfer and Flow Resistance in Cross Flow of Gases over Tube Banks," *Trans. ASME*, vol. 60, p. 384, 1938.
- [18] J. P. Holman, Heat transfer, New-York: McGraw-Hill, 2010.
- [19] R. K. Shah and L. A. London, Laminar Flow: Forced Convection in Ducts, NewYork: Academic Press, 1978.
- [20] D. E. Metzger, "Developing Heat Transfer in Rectangular Ducts With Staggered Arrays of Short Pin Fins," in *ASME*, 1982.
- [21] H. J. P, Heat Transfer, New York: McGraw-Hill, 2010.
- [22] PTC Mathcad User Guide, Parametric Technology Corporation, 2007.
- [23] ANSYS Fluent User Guide, ANSYS Inc..
- [24] M. G. Khan and A. Fartaj, "A review on microchannel heat exchangers and potential applications," *Int. J. Energy Res.*, vol. 35, pp. 553-582, 2010.
- [25] e. a. Alferi F., "Computational modeling of vortex shedding in water cooling of 3D integrated electronics," *International Journal of Heat and Fluid Flow*, no. 44, pp. 745-755, 2013.
- [26] P. Mao and J. Han, "Fabrication and characterization of 20 nm planar nanofluidic channels by glass-glass and glass-silicon bonding," *Lab on a Chip*, vol. 5, no. 8, pp. 837-844, 2005.
- [27] M. Gad-el-Hak, "The fluid mechanics of microdevices – the Freeman scholar," *Journal of Fluids Engennering*, vol. 121, pp. 5-33, 1999.
- [28] E. W. Lemmon, M. O. McLinden and D. G. Friend, "Thermophysical Properties of Fluid Systems," in *NIST Chemistry WebBook, NIST Standard Reference Database Number 69*, Gaithersburg MD, 20899,, National Institute of Standards and Technology,, 2015.

APPENDIXES

APPENDIX A – GENERAL SUPPLEMENTARY INFORMATION

Table A-1 | Flow regimes classification based on the value of the Knudsen number [27].

Knudsen number range	Corresponding flow regime	NS equation validity
$Kn \leq 10^{-3}$	no slip flow	valid
$10^{-3} \leq Kn \leq 10^{-1}$	slip flow	
$10^{-1} \leq Kn \leq 10$	transitional flow	not valid
$Kn > 10$:	free molecular flow	

Table A-2 | Heat transfer convection coefficient and fluid flow friction factor for fully developed laminar flow in ducts of various cross sections. Average Nusselt numbers are based on the cross sectional hydraulic diameter [18].

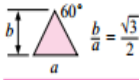
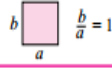

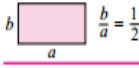

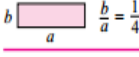
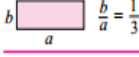
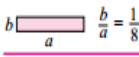

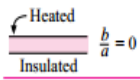
Geometry ($L/D_h > 100$)	Nu_H Constant axial wall heat flux	Nu_T Constant axial wall temperature	$f Re_{D_H}/4$
 $\frac{b}{a} = \frac{\sqrt{3}}{2}$	3.111	2.47	13.333
 $\frac{b}{a} = 1$	3.608	2.976	14.227
	4.002	3.34	15.054
 $\frac{b}{a} = \frac{1}{2}$	4.123	3.391	15.548
	4.364	3.657	16.000
 $\frac{b}{a} = \frac{1}{4}$	5.331	4.44	18.23
 $\frac{b}{a} = \frac{1}{3}$	4.79	3.96	17.25
 $\frac{b}{a} = \frac{1}{8}$	6.490	5.597	20.585
 $\frac{b}{a} = 0$	8.235	7.541	24.000
 $\frac{b}{a} = 0$	5.385	4.861	24.000

Table A-3 | List of parameters influencing the microcooler performance.

Parameter	Influence low stream pressure loss	Influence total heat transfer	Value	Considerations
w_{HE}	no	yes	10 [mm]	Device size
L_{HE}	yes	yes	27.5[mm]	
t_w	no	yes	0.2 [mm]	Minimum axial heat losses
k_w	no	yes	1.2 [Wm ⁻¹ K ⁻¹]	
y_H	no	yes	optimization	50 [μm] minimum to avoid channels clogging
y_L	yes	yes		
d_H	no	yes		
d_L	yes	yes		
\dot{m}	yes	yes		

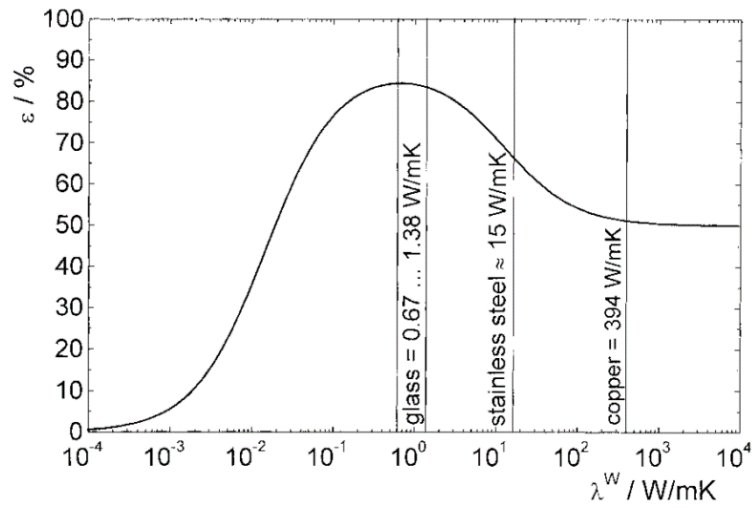


Figure A-1 | Axial heat conduction effect within the separating wall of a microscale heat exchanger. The HE effectiveness value depends on the wall material conductivity. Optimal performance achieved for wall made of glass like materials, having thermal conductivity of about 1 [Wm⁻¹K⁻¹].

APPENDIX B – MATERIAL PROPERTIES

Table B-1 | Various combinations of nitrogen initial conditions at point 2 (**Figure 1a**), that are required for isenthalpic expansion that leads to coolant liquefaction at point 3 with ~ 80 [K] and ~ 0 [psig], [28].

Initial Pressure [psig]	Initial Temperature [K]
500	131
1000	151.8
2300	170.4
3000	173.8
3500	175

Table B-2 | Schott D 263® T ECO glass properties, [16].

Material property	Manufacturer claim
Young Modulus [GPa]	64
Poisson's Ratio	0.2
Bending Strength [MPa]	25
Thermal Conductivity [$W m^{-2} K^{-1}$]	1.2
Specific Heat Capacity [$J kg^{-1} K^{-1}$]	830

Table B-1 | Nitrogen mean properties of high and low stream, for approximate calculations, [28].

Property	High stream	Low stream
$\rho [kg/m^3]$	306.11	2.95
$C_p [J kg^{-1} K^{-1}]$	1684	1058
$k [W m^{-1} K^{-1}]$	0.042	0.017
$\mu [\mu Pa \cdot s]$	25.38	11.6

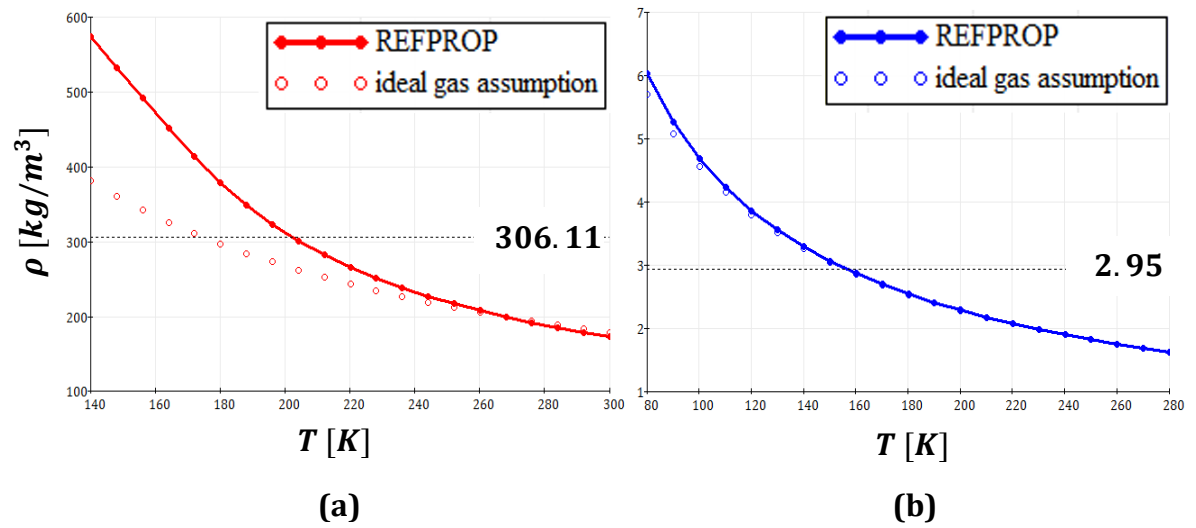


Figure B-1 | Nitrogen density for **(a)** high and **(b)** low stream, 2300[psia] and 20[psia] respectively. It is noted that ideal gas assumption is holding for the low stream, while for the high stream it produces significant error, [28].

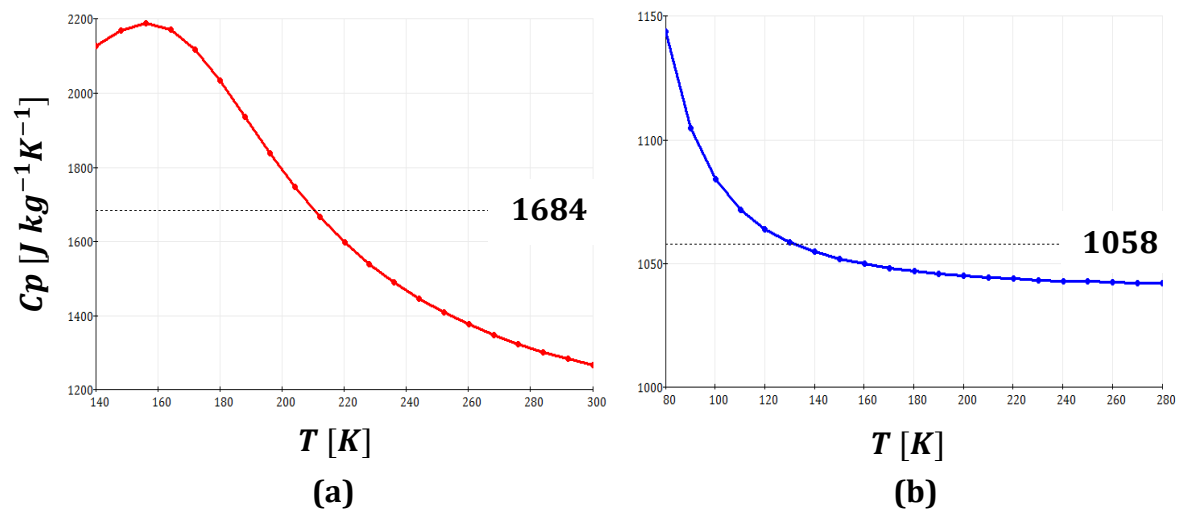


Figure B-2 | Nitrogen specific heat capacity for **(a)** high and **(b)** low stream, 2300[psia] and 20[psia] respectively. It is noted that high pressure stream have higher heat capacity at all considered temperatures, [28].

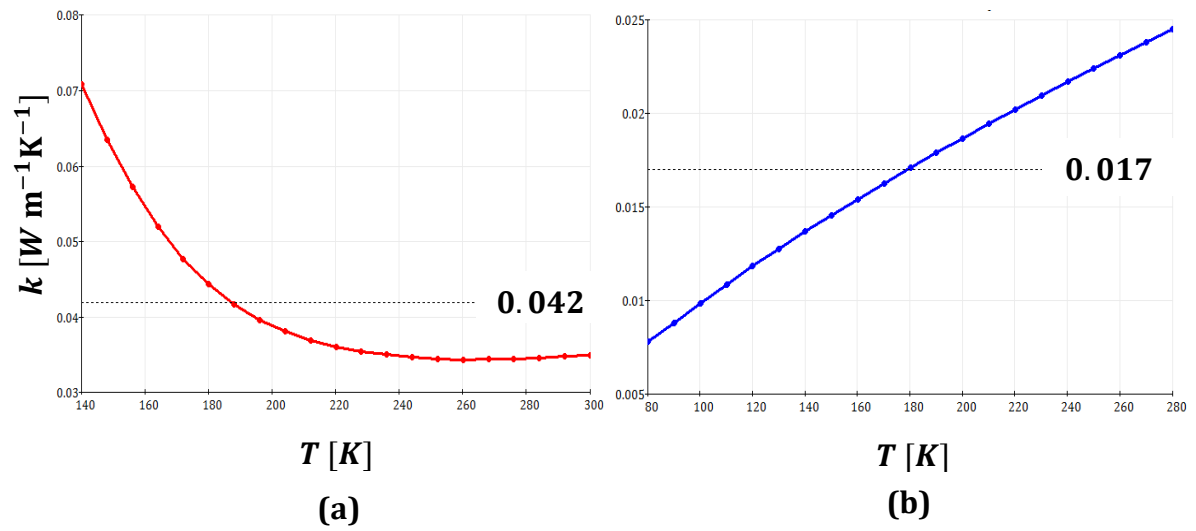


Figure B-3 | Nitrogen thermal conductivity for (a) high and (b) low stream, 2300[psia] and 20[psia] respectively, [28].

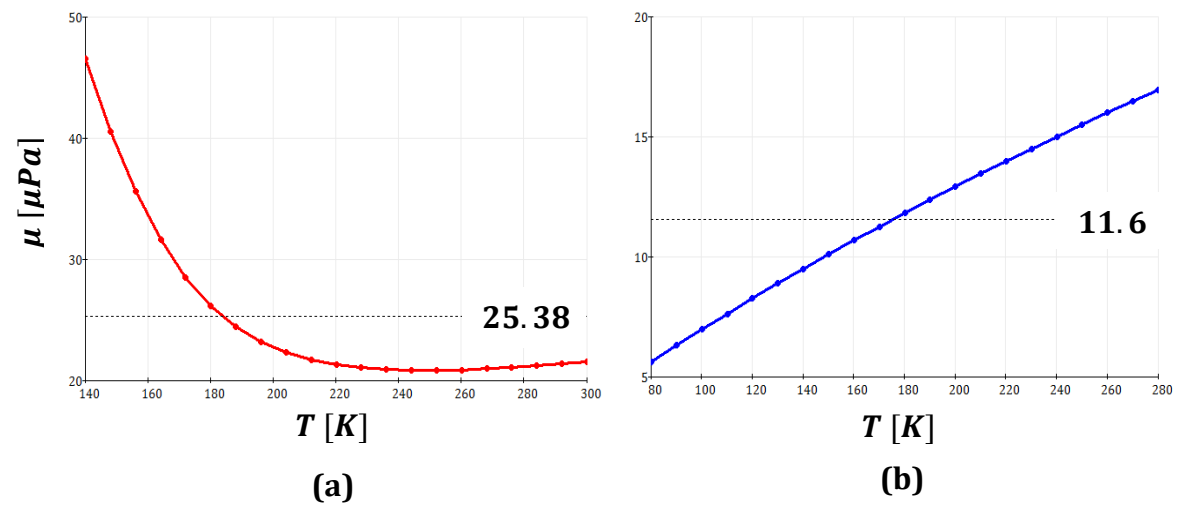


Figure B-4 | Nitrogen dynamic viscosity for (a) high and (b) low stream, 2300[psia] and 20[psia] respectively, [28].

APPENDIX C – ESTIMATION OF RADIATIVE HEAT TRANSFER INTERACTION

During the tests, the temperature at points 3 and 4 were recorded for each level of operating pressure. Using acquired data, we can calculate the low stream radiation heat transfer interaction with the surroundings. We assume a linear temperature distribution along the cooler wall between the two measured points. Radiation heat transfer, for case of varying wall temperature, is calculated using the following relation

$$\dot{q}_{rad} = \epsilon \sigma_b W_{HE} \int_0^{L_{HE}} (T_{wall}^4(x) - T_{ref}^4) dx \quad (C-1)$$

when ϵ is glass emissivity with value about 0.8, $\sigma_b = 5.6703 \times 10^{-8} [Wm^{-2}K^{-4}]$ is Stefan-Boltzmann constant and $T_{wall}(x) = T_3 + \frac{T_4 - T_3}{L}x$. We assume the surroundings having temperature of T_1 . On the other hand, the total heat power can be evaluated from the thermal balance of the low stream

$$\dot{q}_{34} = \dot{m}_f (i_4 - i_3) \quad (C-2)$$

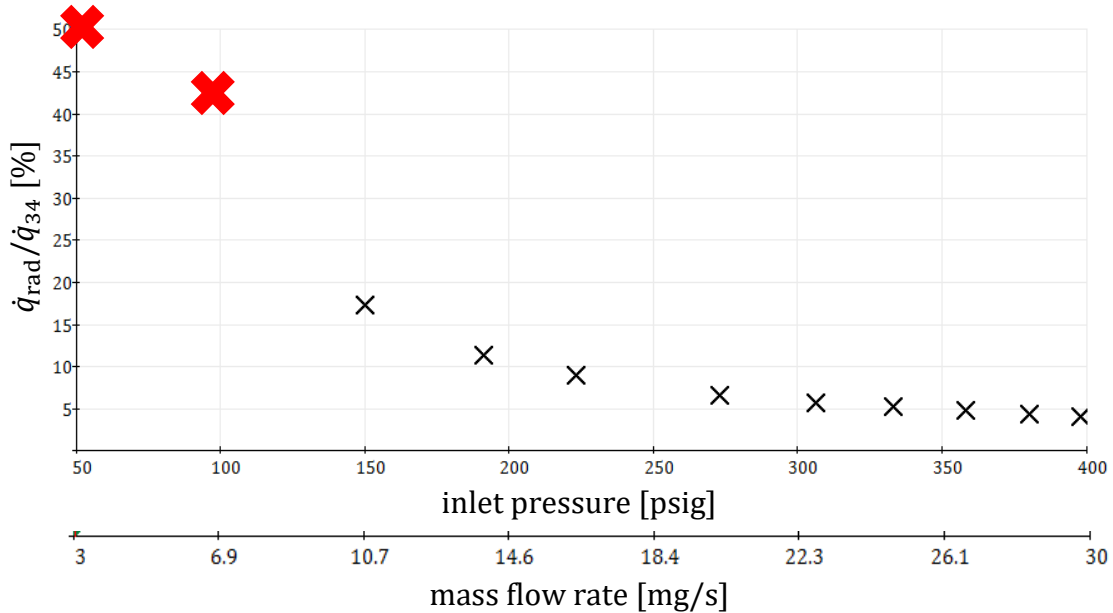


Figure C- 1 | Radiation heat transfer interaction during the performed tests. At experiments with low operating pressure, 54 and 97 [psig], the radiative losses are significant, therefore the perfect insulation assumption, at these experiments does not hold .

Since, low stream collects heat only from two possible sources, the high stream and the environment, by finding the portion of radiation from the total heat interaction, we can evaluate the validity of the thermal insulation assumption.

APPENDIX D – THE NTU METHOD

Getting a meaningful estimation of the pressure loss, requires its calculation based on the coolant local properties, rather using average values. Nitrogen properties dependency on the local temperature is given in APPENDIX B. It's evident that if the density of the low stream is changing by factor of 3, as nitrogen been heated from 80[K] to 300[K], the local Re number undergoes significant change, therefore pressure losses will vary as coolant is advancing within the HE. For that reason, our pressure loss calculation was refined by solving the temperature profile along the HE and using local temperature properties. The temperature profile is obtained by solving differential equations for both streams, neglecting the separating wall. We start from an energy balance for both stream, **Figure D-1**, which for the high stream

$$\dot{m}h_1 = \dot{m}(i_1 - di_H) + U_{tot}w_{HE}(T_H - T_L)dx \quad (D-1)$$

and for the low stream

$$\dot{m}(i_4 - di_L) + U_{tot}w_{HE}(T_H - T_L)dx = \dot{m}i_4 \quad , \quad (D-2)$$

assuming that $di = Cp dT$ we can rewrite these expressions in form of deferential equation of temperature, as dx approaching zero

$$\frac{dT_H}{dx} + \frac{U_{tot}w_{HE}}{\dot{m}Cp_H}(T_L - T_H)dx = 0; B.C | T_H(x = 0) = T_1 \quad (D-3)$$

and

$$\frac{dT_L}{dx} + \frac{U_{tot}w_{HE}}{\dot{m}Cp_L}(T_L - T_H)dx = 0; B.C | T_L(x = L_{HE}) = T_3 \quad , \quad (D-4)$$

replacing with following dimensionless variables:

$$\Theta_i = \frac{T_i - T_3}{T_1 - T_3}; X = \frac{x}{L_{HE}}; NTU_i = \frac{U_{tot}A_{wall}}{\dot{m}Cp_i} \quad ,$$

when the i subscript refers for High and Low stream.

The resulting dimensionless differential equations, are

$$\Theta_H + NTU_H(\Theta_L - \Theta_H)dX = 0; B.C | \Theta_H(X = 0) = 1 \quad (D-5)$$

and

$$\Theta_L + NTU_L(\Theta_L - \Theta_H)dX = 0; B.C | \Theta_L(X = 1) = 0 \quad (D-6)$$

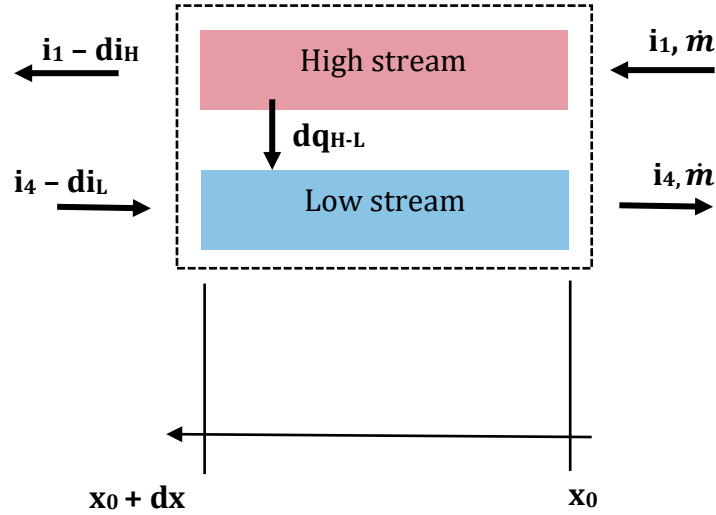


Figure D-1 |Schematics of the HE part of the device for which heat balance calculation performed.

Solution of the system of equations D-5 and D-6, requires transformation of current Boundary Value Problem (BVP) to regular, initial value notation, which can be solved by any commercial mathematical software. After solution, dimensionless temperature has to be transformed back, using Θ_i definition. As a result, the bulk temperature profile along the HE's is obtained and can be used for recalculation of the coolant properties in order to increase the accuracy of pressure loss or other calculations, requiring local nitrogen properties.

APPENDIX E – STRUCTURAL STRENGTH ANALYSIS

It was shown, see paragraph 1.2, that for getting a significant JT cooling effect, the applied pressures must be very large. For this purpose, structural pins were added inside the channels in order to improve the cooler capability to withstand internal pressure loads.

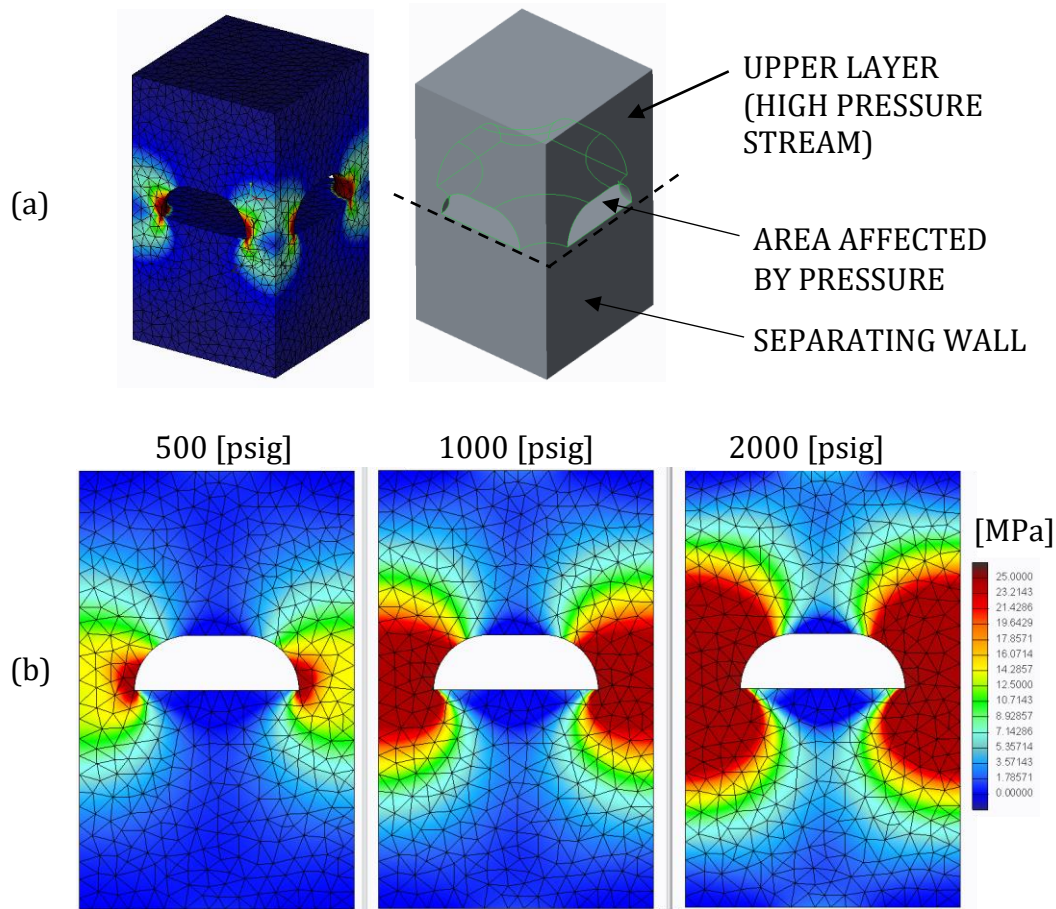


Figure E-1 | (a) Periodic unit cell, containing upper and middle layers of the heat HE's section. **(b)** The results of structural FEA analysis performed for unit cell subjected to a variety of inner pressure magnitudes. Dark red regions corresponds to higher values of tension stresses, rescaled to having maximum at 25 [MPa] level, which is glass maximum permissible tension stress, reported by the manufacturer [16].

In order to estimate the maximum pressure, the device can withstand without mechanical failure, we constructed a simple model for the finite elements analysis (FEA), depicted in **Figure E-1a**. The model represents a periodic cell that is formed of a pattern of evenly spaced pins in aligned formation and found in the high stream of the HE. The pressure inside the high stream of the HE is the operating pressure, that is the maximum pressure inside the device. Thus, this section has to hold

pressures of about 2300[psig]. This pressure that acts on an area of $S_w \times S_w - \pi d^2/4$ in size affects the structure by causing bending of the channels in addition tensile stresses that tend to separate between the bonded glass layers within the microchannel section that are connected through the array of pins. The intermediate glass layer, having thickness of 0.21[mm] was found to be strong enough, but the microscale pins, having diameter of 100[μm], are too small to hold the required pressures. During the analysis of the device structural strength, we varied internal pressure within reasonable limits and obtained the principal stress maps of the unit cell section for the corresponding pressure levels. **Figure E-1b**, shows stress map for pressure magnitude of 2000, 1000 and 500[psig]. The design threshold of 25[MPa] maximal tensile strength is violated for all considered cases, leaving us with some hope for the smallest pressure case. The first three manufactured prototypes were subjected to burst tests, during which, two devices were failed at pressures of about 400 [psig]. The last device survived a pressure of 900[psig] and failed at higher level. It was decided to proceed with study main goal – verifying the optimization procedure, while future works will address the structure improving methods, among the other ideas, by using state of the art ceramic printing processes, lately developed to work with low conductivity, high strength ceramics as Zirconia.

APPENDIX F – CHIP MANUFACTURING

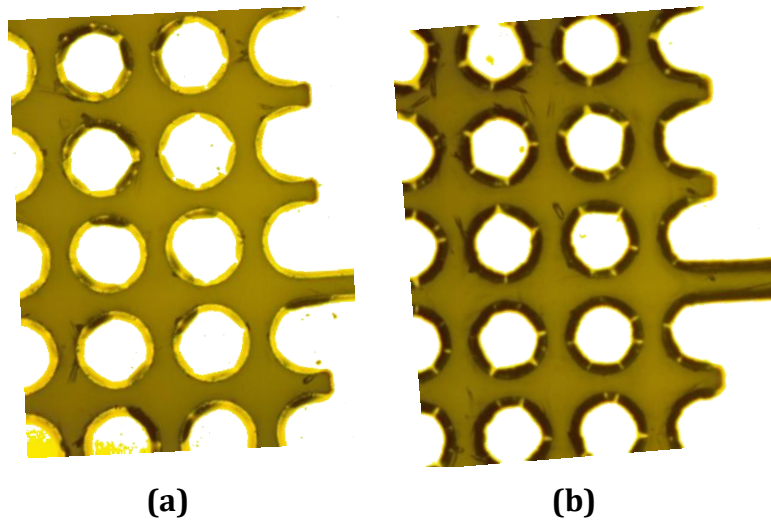


Figure F-1 | The effect of the exposure time of the wafer to HF acid at 49[%] concentration: **(a)** Exposure of 60 [sec], results in high quality circular pins. **(b)** Exposure of 90 [sec], results in degradation of the pins round shape.

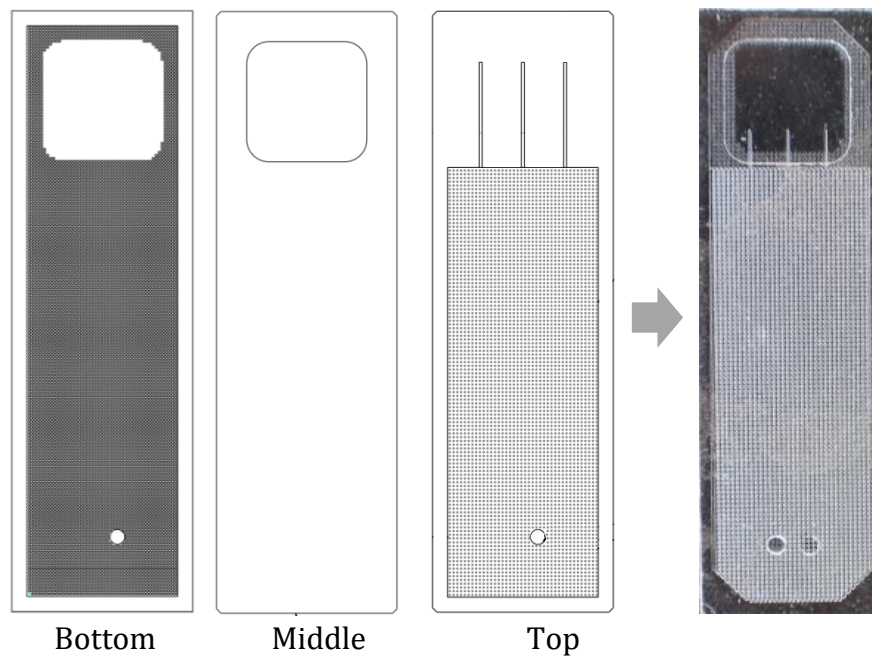


Figure F-2 | The various parts of the microcooler assembly. Bottom – contains the low stream channel and pins, middle – plain piece of glass serves as both the separating wall and expansion chamber where heat absorption occurs. Top- containing the high stream channel with structural pins and additional straight and narrow channels (orifices) for the throttling process. The rightmost part depicted the assembled device.

מעבר החום בהסעה וכן מפלי הלחץ חושבו בעזרת קשרים ניסיוניים ואנליטיים, המופיעים בספרות. תוצאות האנליזה נבדקו בעזרת סימולציות CFD, שבוצעו בתוכנת Fluent של חברת ANSYS. לפי הנתונים שהתקבלו תוכנן וייצר אב טיפוס, עשוי שלוש שכבות מזכוכית D 263@ T של חברת Schott, בעזרת שיטת ייצור בפוטוליטוגרפיה שמשלבת, איכול כימי של הזכוכית בעזרת חומצה הידרופלואורית וחיבורן בתהליך תרמי שהותאם לשימוש בסוג זכוכית זו. האב טיפוס נבחן במערך ייעודי שהוקם, בו ההתקן הוחזק במתאם מיוחד ששימש לקיבוע והספקת גז יחד, עשוי מפלדה עם מוליכות תרמית נמוכה להקטנת ההפסדים. הבחינה התבצעה באווירת וואקום להקטנת הפסדי חום בהסעה, כך שלמעשה בוצע ניסיון להתקרר, כמה שיותר, לתנאי בידוד תרמי מושלם. בנוסף לקביעת תכונות החנקן בכניסה להתקן, טמפרטורות נוספות נמדדו על גבי המחליף החום ותוצאתם הושוואו לאנליזת CFD, אשר נמצאה בהתאמה טובה מאוד למידע שנאגר בניסוי.

תכן מערכות אופטיות בתחום האינפרא-אדום, דורש מהמתכננים שימוש בהתקן לקירור קריוגני של מטריצת הגלאי. קירור הגלאי לטמפרטורות נמוכות אלו נדרש על מנת לקבל איכות אופטית טובה של האובייקט הנבחן ובכך למלא את ייעוד המערכת. במערכות מוטסות, במיוחד חד פעמיות, לדוגמא טילים, בנוסף לפונקציונליות נדרש מההתקן משקל נמוך, ממדים קטנים ומחיר נמוך. זוג מדענים ב-1852 בשם ג'יימס ג'ול וויליאם תומסון גילו את האפקט, הקרוי על שמם, והוא מתאר ירידת טמפרטורה של גז, אשר מתפשט מלחץ גבוה ללחץ נמוך, בתהליך אדיאבטי בתוך שסתום התפשטות. ההתקן הראשון, שתפקידו היה לגרום לניזול של הגז העובר דרכו, והמבוסס על האפקט החדש, הוגש לפטנט בשנת 1895 ע"י שני מדענים, כל אחד בנפרד, וויליאם האמפסון וקארל וון לינדה. ההתקן כלל שלושה רכיבים עיקריים, מחליף חום בשיטת זרימה נגדית, שסתום התפשטות ומיכל בו נאגר הגז הניזול. מכון שאפקט הקירור חלש יחסית, תהליך הקירור נעשה בשיטה רגנרטיבית, כאשר הגז הקר, שעדיין לא הגיע לטמפרטורת הניזול במעבר דרך השסתום בפעם הראשונה, החליף חום עם הגז בכניסה לשסתום, קירר אותו, עד שלאחר מספר מעברים בשסתום, הגז מגיע לטמפרטורת הניזול. כמובן כמה שמחליף החום אפקטיבי יותר, נדרשו מספר קטן יותר של מעברים, עד להשגת הניזול. פרק זמן מרגע הפעלת המערכת עד לניזול, נקרא – זמן ניזול והוא פרמטר חשוב. מקרר מסוג זה, נחקר רבות ע"י מכוני מחקר באנגליה וארה"ב החל מאמצע המאה ה-20 לטובת שילוב במערכות אופטיות מבצעיות. בשנות ה-80, בעקבות כניסתה של טכנולוגיית הליתוגרפיה לייצור התקנים ממוזערים, נפתח כיוון חדש לחקר של תופעות מעבר חום וזרימה בהתקנים מיקרו וננו. כתוצאה מכך החלו להופיע דיווחים על תופעות חדשות, שלא היו קיימות בהתקנים ומחליפי חום בפרט, בגדלים קונבנציונליים.

בעבודה זו חקרנו תופעות וביצועים של מקרר בשיטת ג'אול-תומסון זעיר, המופעל על ידי גז חנקן שנכנס להתקן בלחץ 2300 [psig] וטמפרטורת ניזול של 80 [K] , כאשר מחליף החום הינו של זרימה נגדית ששולבו לתוכו מיקרו פינים. תפקיד הפינים, שקוטרם כ-100 מיקרון, הינו לחזק מבחינה מבנית את התעלות של מחליף החום מצד אחד ולשפר את מקדם מעבר החום בהסעה, מצד השני, וזאת ע"י יצירת הפרעה לזרימה.

גאומטריית הפינים, קוטר וגובה, וכן ספקת החנקן דרך ההתקן נקבעו בעזרת אופטימיזציה פרמטרית שנעשתה, על מנת לשפר את יכולת קליטת החום של ההתקן, תוך שמירה על מגבלות הפסדי הלחץ בתוכו. בעיית מעבר החום, נפתרה באופן מקורב בשיטת ה-NTU, כאשר מקדמי

המחקר נעשה בהנחיית פרופסור חבר גלעד יוסיפון ראש מעבדה למיקרו וננו-זרימה בפקולטה להנדסת מכונות, טכניון. אני מודה לטכניון – מרכז לחקר החלל (ASRI) על שם נורמן והלן אשר, קרן טכניון לחקר האבטחה (CSST) וחברת רפאל – מערכות הגנה בע"מ, על מימון הנדיב שניתן למחקר זה.

הגברת מעבר החום במחליף חום זרימה נגדית המשולב במיקרו-מקרר קריוגני מבוסס אפקט ג'אול-תומסון

חיבור על מחקר
לשם מילוי חלקי של הדרישות לקבלת התואר מגיסטר למדעים
בהנדסת מכונות

פריימן לאוניד